

2015

Coarse-Grained Molecular Dynamics Modeling of Interactions between Biomolecules and Nanostructures

Yihua Zhou
Lehigh University

Follow this and additional works at: <http://preserve.lehigh.edu/etd>

 Part of the [Mechanical Engineering Commons](#)

Recommended Citation

Zhou, Yihua, "Coarse-Grained Molecular Dynamics Modeling of Interactions between Biomolecules and Nanostructures" (2015).
Theses and Dissertations. 2911.
<http://preserve.lehigh.edu/etd/2911>

This Dissertation is brought to you for free and open access by Lehigh Preserve. It has been accepted for inclusion in Theses and Dissertations by an authorized administrator of Lehigh Preserve. For more information, please contact preserve@lehigh.edu.

**Coarse-Grained Molecular Dynamics Modeling of Interactions between
Biomolecules and Nanostructures**

by

Yihua Zhou

A Dissertation

Presented to the Graduate and Research Committee

of Lehigh University

in Candidacy for the Degree of

Doctor of Philosophy

in

Mechanical Engineering

Lehigh University

August 2015

© (2015) Copyright

(Yihua Zhou)

DISSERTATION SIGNATURE SHEET for Yihua Zhou

Approved and recommended for acceptance as a dissertation in partial fulfillment of the requirements for the degree of Doctor of Philosophy

Yihua Zhou

Coarse-Grained Molecular Dynamics Modeling of Interactions between Biomolecules and Nanostructures

April 29, 2015

Defense Date

Aug 4, 2015

Approved Date

Dissertation Director
(Must Sign with Blue Ink)

Committee Members:

(Dr. Yaling Liu)

(Dr. Edmund Webb III)

(Dr. Jeetain Mittal)

(Dr. Dimitrios Vavylonis)

ACKNOWLEDGMENTS

First, I would like to express my greatest appreciation to my advisor, Dr. Yaing Liu, for his continuous support, encouragement, motivation, and guidance. Without his direction and support, this work would not have been possible.

My sincere thanks are extended to my committee members, Dr. Jeetain Mittal, Dr. Edmund Webb, and Dr. Dimitrios Vavylonis. Thank you for your time, encouragement, valuable advices, and wonderful classes you gave, especially for your understandings when unpredicted accident happens.

Special thanks go to Dr. Yue Yu, who gave me a lot of valuable advice on defense experience. I would also like to thank my friend Yajun Ding, who was always willing to help and give his best suggestions.

Many thanks are delivered to other colleagues in the laboratory for their helpful discussion, including but not limited to Jifu Tan, Shunqiang Wang, Christopher Uhl, Salman Sohrabi, Doruk Yunus and Antony Thomas. My research would not have been so smooth without their helps.

I would also like to thank my parents for having brought me up. They were always supporting me and encouraging me with their best wishes. Finally, I would like to thank my boyfriend, Hanqi Liu. He was always there cheering me up and stood by me through the good times and bad.

TABLE OF CONTENTS

LIST OF TABLES	ix
LIST OF FIGURES	x
ABSTRACT	1
1. Introduction to Coarse-Grained Molecular Dynamics	4
1.1. Background information.....	4
1.2. Interaction function and force fields	7
1.3. Theoretical frameworks to coarse-graining method.....	8
1.3.1. Elastic Network Models (ENMs)	9
1.3.2. Freely jointed chain (FJC) polymer model.....	9
1.3.3. The MARTINI force field	10
1.3.4. Bottom-up method for setting up theoretical framework.....	12
1.4. Model formulation of coarse-graining method	12
1.4.1. Set up the coarse-grained topological model.....	13
1.4.2. Characterize potentials for the system.....	13
1.4.3. Obtain potential parameters from all-atom models	14
1.4.4. Validation of coarse-grained models	14
1.5. Algorithm flowchart for the coarse-grained molecular dynamics	14
2. Biomarker Binding on an Antibody-Functionalized Biosensor Surface	16

2.1.	Introduction.....	16
2.2.	Methods.....	18
2.2.1.	CG topology.....	18
2.2.2.	CG potentials	22
2.2.3.	Validation of CG model.....	23
2.3.	Results and Discussions.....	26
2.3.1.	Effect of surface properties	27
2.3.2.	Effects of electric field strength	30
2.3.3.	Effects of surface coating density	33
2.4.	Conclusions.....	34
2.5.	Acknowledgements.....	36
3.	Mechanical properties of nanoworm assembled by DNA and nanoparticle conjugates	37
3.1.	Introduction.....	37
3.2.	Methods.....	40
3.3.	Results & Discussions.....	46
3.3.1.	Snapshots for stretching/bending/twisting processes.....	46
3.3.2.	Mechanical properties of the nanoworm	48
3.3.3.	Effects of temperature.....	52

3.3.4.	Effects of DNA coating density.....	53
3.3.5.	Effects of NP sizes.....	55
3.4.	Conclusions.....	56
3.5.	Acknowledgements.....	58
4.	Mechanical response and potential application of nanosheet by DNA-NP conjugates	59
4.1.	Introduction.....	59
4.2.	Methods.....	61
4.3.	Results and Discussions.....	65
4.3.1.	Snapshots for stretching / shearing tests.....	65
4.3.2.	Energy/Force-Extension Curves.....	67
4.3.3.	Effects of DNA Hairpin Loop Structures.....	68
4.3.4.	Numerical Model for Threshold Force Values.....	72
4.3.5.	Temperature/Concentration Scaling Factors.....	73
4.3.6.	Evaluation of numerical model.....	75
4.3.7.	Material properties of nanosheet.....	77
4.4.	Conclusions.....	79
4.5.	Acknowledgements.....	80
REFERENCES	81

Vita.....92

LIST OF TABLES

Table 1. Information of each bead in the CG Ab model.....	20
Table 2. Diffusion coefficients calculated from two models	24
Table 3. Potential parameters between the substrate and other molecules	28
Table 4. Temperature scaling factors.....	74
Table 5. Salt concentration scaling factor	75
Table 6. Comparison between simulation results and numerical results under different situations	76

LIST OF FIGURES

Figure 1. Typical non-bonded potentials. (a) Lennard-Jones potential. (b) The Coulomb Force, Shifted Force and Shift Function $S(r)$, using $r_1 = 2$ and $r_c = 4$	8
Figure 2. Principles and potentials of bond (a), angle (b) and dihedral (c)	8
Figure 3. Mapping between the chemical structure and the coarse grained model for DPPC, cholesterol, and benzene using MARTINI approach [5].....	11
Figure 4. Algorithm flowchart for Coarse-Grained Molecular Dynamics	15
Figure 5. (a) All-atom model of Ab[20]; (b) Detailed topological information of CG Ab model (12 atoms, 4 atom types; 16 bonds, 5 bond types; 16 angles, 5 angle types; 5 dihedrals, 5 dihedral types.); It should be noted that atoms with the same color don't mean they are the same atom type. (c) CG model of Abs.	20
Figure 6. (a) All-atom model of biomarker[47]; (b) Detailed topological information of CG biomarkers (12 atoms, 4 atom types; 14 bonds, 5 bond types; 16 angles, 5 angle types; 5 dihedrals, 5 dihedral types). It should be noted that atoms with the same color don't mean they are the same atom type. (c) CG model of biomarkers.....	21
Figure 7. Simulation system setup. Four Abs are immobilized on the substrate by SAMs, one biomarker is released from a height of 10 nm above Abs.....	22
Figure 8. Schematic of Ab orientation factor. θ varies from 0° to 90° while α is constrained in the range of $[0,1]$. When the Ab is perpendicular to the substrate surface, α is equal to 1 which is best for biomarker binding; when the Ab lies flat on the substrate surface, α is equal to 0 which is not beneficial for biomarker binding.....	26

Figure 9. A typical biomarker binding process. The simulation was run with Ab coating density of $1600/\mu\text{m}^2$, SAM length of 3.2 nm, and electric field strength of 0.1 V/m.27

Figure 10. (a) Orientation factors under different surface interaction types: SA - strong attraction, WA - weak attraction, N - neutral, WR - weak repulsion, and SR - strong repulsion. (b) Biomarkers binding time under different surface interaction types.29

Figure 11. (a) Time history of Abs orientation factors under different conditions. The blue solid line is the time history of Ab orientation factors with an electric field strength of 0.1 V/m and SAM length of 0.8 nm; the black solid line is the time history of Ab orientation factors with an electric field strength of 0.1 V/m and SAM length of 3.2 nm; the red dashed line is the time history of Ab orientation factors without an electric field and SAM length of 0.8 nm; the green dashed line is time history of Ab orientation factors without an electric field and SAM length of 3.2 nm. (b) A typical snap shot of Abs orientation without an electric field. (c) A typical snap shot of Abs orientation with an electric field.....31

Figure 12. (a) Abs orientations under different electric field strengths and different SAM lengths. (b) Biomarker binding times under different electric field strengths and different SAM lengths.32

Figure 13. (a) Effects of surface coating density on Abs orientation factor. (b) Effects of surface coating density on biomarkers binding time.34

Figure 14. CG topological models for (a) coating DNA, (b) DNA-NP conjugate and (c) the nanoworm constructed by conjugates43

Figure 15. Benchmark cases for the CG model. (a) Mechanical properties of DNA by pulling test. (I), (II) and (III) are the physical settings for the tensile test of DNA strands,

the energy/force-extension curves of our model and results reported in Ref.[146], respectively. (b) Internal structure of the dimer assembled by DNA-NP conjugates. (I) is the dimer structure assembled by DNA-NP conjugates, (II) is the comparison of the dependence of inter-particle distance on DNA length (number of DNA bases) of our model and that of Gang *et al.* [147].....44

Figure 16. Loading conditions for the nanoworm in processes of (a) stretching, (b) bending and (c) twisting. D_s , D_b and θ_t represent the stretching displacement, bending displacement, and rotating angles, respectively.....45

Figure 17. Snapshots for the stretching process of a nanoworm. δ represents the extension which equals $L_n - L_0$ ($n = 0, 1, \dots, 5$).....46

Figure 18. Snapshots for the bending process of a nanoworm. δ represents the deflection.47

Figure 19. Snapshots for the twisting process of a nanoworm. θ represents the twisting angles. Strands which still have interparticle linkages are marked as red.....48

Figure 20. Energy and dehybridization ratio variations during different deformation processes: (a) Energy-extension curves of the nanoworm. (b) Diagram of dehybridization ratio to extension under three mechanical processes.....50

Figure 21. Energy variations per strand during the bending process with different NP sizes. (a) Diagram of bending energy per strand versus extensions. (b) Variations of E_{total} , E_{deform} and E_{dehyb} per strand versus extensions.....51

Figure 22. Effects of temperature on stretching property of the nanoworm. (a) Stretching energy versus extension. (b) Effects of temperature on stretching stiffness. (c) Effects of temperature on stretching strength.....	53
Figure 23. Effects of coating density on stretching property of the nanoworm. (a) Stretching energy versus extension. (b) Effects of coating density on stretching stiffness. (c) Effects of coating density on stretching strength.	54
Figure 24. Effects of NP diameters on stretching processes of the nanoworm. (a) Stretching energy versus deflections. (b) Effects of NP diameter on stretching stiffness. (c) Effects of NP diameter on stretching strength.	55
Figure 25. Constructing 2D nanosheet with DNA-NP conjugates. (a) Coating DNA, (b) NP, (c) conjugate, (d) hairpin loop, (e) full nanosheet model, (f) simplified nanosheet model.....	62
Figure 26. Benchmark case for the mechanical behavior of DNA hairpin loop. (a) Initial setup for the hairpin loop stretching. (b) Force/extension curve of our model. (c) Experimental data for force/extension curve[194, 195].....	63
Figure 27. Indentation testing of the 2D nanosheet as a benchmark case. (a) Physical settings for the indentation. (b) Force-displacement curve of our model. (c) Force-displacement curve obtained by Luo <i>et al.</i> [150].....	64
Figure 28. Displacement controlled (a) uni-axial stretching, (b) area expansion and (c) shearing tests of the 2D nanosheet.....	65
Figure 29. Snapshots for area expansion process. For clarity, coating DNAs were hidden	66

Figure 30. Snapshots for the shearing process of the nanosheet. For clarity, coating DNA were hidden	67
Figure 31. (a) Time history of Energy during the stretching and shearing processes. (b) Force-extension curve during the stretching process. (c) Force- shear degree curve during the shearing process	68
Figure 32. Different types of hairpin loop structures and the correspondingly assembled nanosheets. To show how these hairpin loops serve as connections between NPs, the coating DNAs of nanosheets are hidden.....	69
Figure 33. Effects of hairpin loop structures on mechanical properties of nanosheet. (a) Energy-extension curve for stretching process. (b) Energy-strain curves for stretching process. (c) Force-extension curve of the nanosheet for stretching process. (d) Force-shearing degree curve of the nanosheet for shearing process.....	70
Figure 34. Safe level of force range in (a) stretching test and (b) shearing test.....	72
Figure 35. Effects of temperature on Mechanical properties of nanosheet. (a) Effects of temperature on free energies in stretching process. (b) Effects of salt concentration on free energies in shearing process.....	74
Figure 36. (a) Definition of area expansion modulus. (b) Force-strain curve of the nanosheet during area expansion	78
Figure 37. (a) Definition of shear degree. (b) Shear force-shear degree curve of the nanosheet.....	78

ABSTRACT

In modern biotechnology and medicine realm, understanding interactions between biomolecules and nanostructures at molecular level is essential for designs of nanoscale diagnostic or therapeutic devices. Molecular Dynamics simulations have already become a significant and reliable tool to reveal mechanisms of bio-physiological phenomena between bio-nano interfaces. However, due to the limited time and length scales a full-atomistic molecular dynamics system can reach, the coarse-grained molecular dynamics technique is continuously sought to describe interactions between biomolecules and nanostructures. Here, the coarse-grained molecular dynamics is applied to different cases for revealing complex interactions between biomolecules and nanostructures.

The first case in this dissertation is to quantify the biomarker detection process, solve the puzzle of biosensor detection at ultralow concentration and expedite the technique of early cancer diagnosis. Antibodies have been used as bioreceptors in bio-diagnostic devices for decades, whose performances are affected by various factors such as orientation, density, and local environment. While there are extensive works on designing and fabrication of various biosensors, little is known about the molecular level interactions between antibodies coated on sensor surfaces and biomarkers suspended in medium. Thus, a coarse-grained model for biomarkers binding on an antibody-functionalized biosensor surface is constructed to study effects of surface properties and external parameters on antibody orientation and biomarkers binding time. The surface interaction type is found to significantly influence the antibody orientation and biomarker binding time. A proper

electric field range is discovered to not only well-orientate antibodies but also steer biomarkers toward the surface, consequently reducing the binding time of biomarkers by two orders of magnitude. Moreover, a suitable surface coating density of antibodies has been proposed to help antibody orientation as well as biomarker binding. These findings can be used for rational design of biosensors with higher efficiency and more sensitive detections.

For the subsequent cases, the coarse-grained molecular dynamics model for the DNA-NP conjugate which is assembled by DNA and nanoparticles is established and used as building blocks for constructing one dimensional nanoworm and two dimensional nanosheet structures. Their mechanical properties are tested and potential applications are discussed with the developed model.

The nanoworm structure, which can be applied in fields of drug targeting, image probing and thermal therapies, has been assembled by DNA-nanoparticle conjugates. Subsequently, its mechanical properties have been investigated due to their importance on the structural stability, transport and circulations of the nanoworm. Stiffness and strengths of the nanoworm under different deformation types are studied by coarse-grained molecular dynamics simulations. Effects of temperature, DNA coating density and particle size on mechanical properties of nanoworms are also thoroughly investigated. Results show that both resistance and strength of the nanoworm are the weakest along the axial direction, indicating it is more prone to be ruptured by a stretching force. In addition, DNA strands are found to be more important than nanoparticles in determining mechanical properties of the nanoworm. Moreover, both strength and resistance in regardless of directions are proved to be enhanced by decreasing the temperature, raising the DNA coating density and

enlarging the particle size. This study is capable of serving as guidance for designing nanoworms with optimal mechanical strengths for applications.

Two dimensional arrays of DNA-nanoparticle conjugates have also been fabricated and become a promising platform for developments of chemical sensor, molecular circuit, and mechanical analysis tools. Whatever it is used for, the mechanical properties affect its efficiency and efficacy in large extent. Thus, its mechanical properties have been scrutinized by the coarse-grained molecular dynamics simulation model. Stress-strain curves of the lattice under shearing and stretching are obtained and analyzed. Different hairpin structures have been used to connect adjacent DNA-nanoparticle conjugates and proven to influence stress-strain relationship of 2D array. Effects of physical conditions such as the temperature and salt concentration on mechanical properties of the 2D lattice are also investigated. Results found that 2D lattice behave like a macroscopic paper or alumina foil, whose force-displacement curve is in great agreement with that of elastic sheet. The 2D nanosheet is quite stable at 293 K with a salt concentration of 100 mM. Based on aforementioned results, a numerical model is proposed for the stress-strain relationship of 2D array. In future, this numerical model will be evaluated by our experimental results.

Future work includes the investigation on mechanical response of three dimensional nanocrystal constructed by the same DNA-NP conjugates and a multiscale modeling of red blood cell membrane rupturing process.

1. Introduction to Coarse-Grained Molecular Dynamics

1.1. Background information

In modern biotechnology and medicine realm, understanding interactions between biomolecules and nanostructures are essential for design of many applications including lab-on-a-chip[1,2] devices for biomolecular analysis[3], nanoparticle-based diagnostics [4], implants[5, 6] and drug delivery techniques. However, the development of nanoscale diagnostic or therapeutic devices as well as toxicity assessment is hindered by several central questions: (i) development of atomistic and coarse-grained force fields governing the interaction of inorganic materials with proteins, lipids, DNA and outer cell surfaces, (ii) development of coarse-grained models for biomolecules forming the interface such as proteins, glycoproteins, glycolipids, and lipids, (iii) prediction of the energetics and kinetics of the adsorption of these materials at the interface, and (iv) modeling the structure and dynamics or nanoparticle protein corona. To address above tasks, a quantitative description of interaction between engineered nanomaterials and bio-interfaces is required.

The major obstacle for the successful implementation of the bio-nanotechnologies in medicine is the poor understanding of protein-nanomaterials interactions. The properties of the nanomaterials when they get in contact with proteins are completely different from the original surfaces of the nanomaterials. This new biological identity of the nanomaterials is formed via the creation of a new interface between the nanomaterials and the biological medium, which is referred to as the bio-nano interface. It seems that methodological issues are essential for the predictive description of interactions at the bio-nano interface.

A crucial stimuli for the function of these devices is understanding the interaction between biomolecules and nanostructures clearly. Molecular dynamics (MD) is well established and widely used for investigating the molecular details of biomolecules and nanostructures. Its simulation results are not only flexible for us to test assumption/theoretical models but also inspire us with interesting phenomenon. However, due to the huge structural information of biomolecules and limited computer power, MD can only study systems with very small length-scale and time-scale, far less than expected [7].

A key factor for the simulations is the enormous range of involved time and length scales. Biomolecule-nanostructure interface systems span length scales from atomistic sub-nanometer distances to hundreds of nanometers. From time scale aspect, the protein adsorption and desorption is with a corresponding timescale of milliseconds while the membrane rearrangement can take even longer. Considering the limited time and length scales that Molecular Dynamics can reach, the development of coarse-grained models and multiscale methods for these systems is of primary importance. However, it is still challenging to model the biomolecule-nanostructure interactions because researchers lack consistent, accurate and universal force fields both at atomistic and coarse-grained level. Thus, a joint effort have been paid for filling the gaps in molecular level knowledge and understanding the essential interactions at bio-nano interface Although it is unrealistic to model the complete details of bio-nano interface, the most crucial stage of the process can be focused.

The idea of using a simplified model in computational studies of biomolecules was first proposed by Levitt & Warshel for protein folding [8]. Then a much simpler $\bar{G}O$ model emerged at the same year and successfully solved problems of protein folding, unfolding and

fluctuation [9]. This idea grew into the coarse graining method quickly and now is widely used by researchers because of its potential of extending the length and time scale of the system that can be studied. Coarse-graining approach not only makes the simulation faster due to fewer particles and interactions, but also has a faster dynamics due to lower frictional forces of the smoother potential [10]. Only the interesting degrees of freedom and main physics of given system are preserved in the coarse-grained model simulation. With detailed information that doesn't account for the physics to be studied wiped off, the coarse-grained complex physical systems can be simulated over large time and length scale which cannot be accessed by all-atom models..

Not all systems will benefit from a coarse-grained modeling. For some systems and some specific phenomenon, all-atom modeling may be required. Before we decide to use coarse-grained approach, we must consider whether it is necessary. Cases calling for the coarse-grained approach include: (1) unreachable time scale for phenomenon or behavior via all-atom modeling; (2) inaccessible length scale of the system via all-atom modeling [11]; (3) the studied points are global system properties and/or mechanical behavior rather than molecular structure and/or chemical interactions; (4) the results got from coarse-grained model have no difference from that from all-atom model but the simulation is much more effective.

After the coarse-graining approach is determined to be utilized for the research, the coarse-graining method should be selected. To make a right choice for the coarse-grained modeling and potentials, the theoretical frameworks to the coarse-graining method need to be understood, which will be explained informatively. The selection of a coarse-grained model depends on bio-behaviors to be studied. The same biomolecule can be coarse-grained

into different models if different phenomena are studied; the applied potentials also vary as different interactions/mechanics are focused. The required elements in a good coarse-graining framework contain: (1) appropriate coarse-grained topological model for the system; (2) proper coarse-grained potentials to define and characterize the bio-system; (3) suitable parameters for potentials obtained from all-atom model; (4) validation of coarse-grained model [11].

Even a sea of attempts have been tried to use coarse-grained molecular dynamics to study the interfacial phenomena between biomolecules and nanostructures, it is still a big challenge to reproduce any phenomenon in the field of bio-nanotechnology due to the complex system and obscure interactions between each other. In order to utilize coarse-graining method better and capture more essence of all kinds of biomolecule-nanostructure interaction, the theoretical framework and model formulation have been explained in detail, following a short extension that study mechanical properties of a novel membrane with nanopores made up of coarse-grained DNA model.

1.2. Interaction function and force fields

Usually the potential functions can be subdivided into three parts:

Non-bonded: Lennard-Jones or Buckingham, and Coulomb or modified Coulomb, as shown in Figure 1. The nonbonded interactions are computed on the basis of a neighbor list (a list of non-bonded atoms within a certain radius), in which exclusions are already removed.

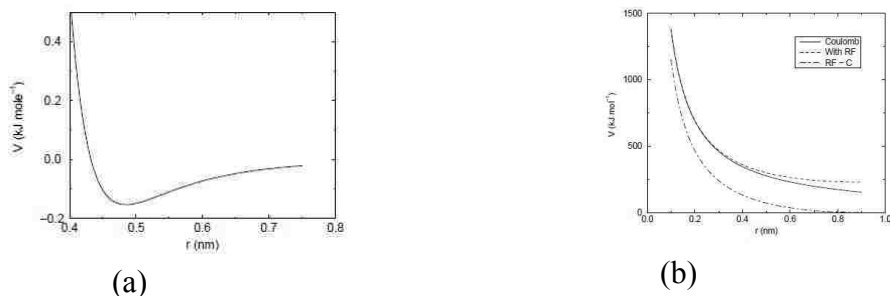


Figure 1. Typical non-bonded potentials. (a) Lennard-Jones potential. (b) The Coulomb Force, Shifted Force and Shift Function $S(r)$, using $r_1 = 2$ and $r_c = 4$.

Bonded: covalent bond-stretching, angle-bending, improper dihedrals, and proper dihedrals, as shown in Figure 2. These are computed on the basis of fixed lists.

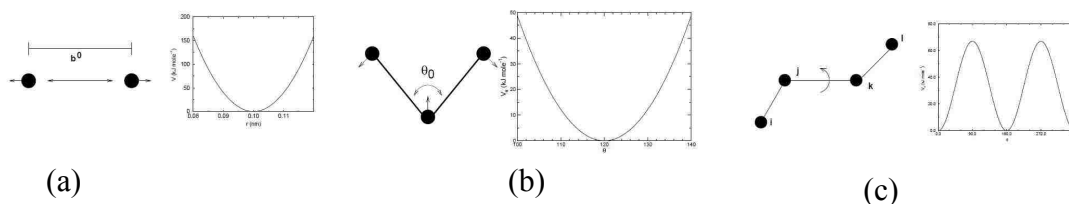


Figure 2. Principles and potentials of bond (a), angle (b) and dihedral (c)

Restraints: position restraints, angle restraints, distance restraints, orientation restraints and dihedral restraints, all based on fixed lists.

1.3. Theoretical frameworks to coarse-graining method

Various methods for coarse-graining complex physical systems have been tried for describing the biomolecule-nanostructure interaction more appropriately. Each method has its own unique characteristics and principles. In overall, all types of coarse-graining methods establish models by regarding various residues as different beads; the differences lie on how

to describe interactions of intra-molecules and inter-molecules. Due to a limited length of this report, the theoretical frameworks of only a few most popular ones will be discussed.

1.3.1. Elastic Network Models (ENMs)

ENMs are the simplest form of coarse-grained model with single uniform harmonic potentials instead of detailed atomic potentials between residues. They only consider intramolecular interactions, relating to the displacement for atom pair i and j under isotropy assumption:

$$E_{\text{CG-ENM}} = \sum \phi_{\text{ENM}}(r) \quad (\text{Eqn. 1})$$

where

$$\phi_{\text{ENM}}(r) = \frac{1}{2} K_r (r - r_0)^2 \quad (\text{Eqn. 2})$$

Here the interaction of each pair of atoms is regarded as a harmonic spring bond with stiffness K_r and an initial equilibrium distance r_0 [11]. Different K_r and r_0 values are assigned for different types of interaction.

The biggest advantage of ENMs is simple, but they lack the necessary description for inter-molecules interactions and large deformation from equilibrium conditions. If the intermolecule interactions are the concerns of research, other coarse-graining methods should be taken.

1.3.2. Freely jointed chain (FJC) polymer model

A freely jointed representation for protein macromolecules is a combination of intramolecule interaction and intermolecule interaction [11], which can be described as below:

$$E_{CG-FJC} = E_{\text{bonded}} + E_{\text{nonbonded}} = \sum \phi_{\text{FENE}}(r) + \sum \phi_{\text{WAC}}(r) \quad (\text{Eqn. 3})$$

The finitely extensible nonlinear elastic (FENE) potential is used for connected beads and prevents polymer chains from crossing each other:

$$\begin{aligned} \phi_{\text{FENE}}(r) &= -\frac{1}{2}kr_0^2 \ln[1 - (\frac{r}{r_0})^2] & \text{for } r < r_0 \\ \phi_{\text{FENE}}(r) &= 0 & \text{for } r \geq r_0 \end{aligned} \quad (\text{Eqn. 4})$$

The WAC potential is the transformation of Lennard-Jones potential truncated at the position of the minimum and shifted to zero (ensuring a pure repulsion between molecules) thereafter:

$$\begin{aligned} \phi_{\text{WAC}}(r) &= 4\epsilon[(\frac{\sigma}{r})^{12} - (\frac{\sigma}{r})^6] & \text{for } \frac{r}{\sigma} < \sqrt[6]{2} \\ \phi_{\text{WAC}}(r) &= 0 & \text{for } \frac{r}{\sigma} \geq \sqrt[6]{2} \end{aligned} \quad (\text{Eqn. 5})$$

FJC potential is suitable for long-chain polymers with relative short persistent lengths. But polymers created as FJC model are completely straight and unstretchable, disorder can only happen at joints.

1.3.3. The MARTINI force field

Based on the fact that all proteins are composed of 20 different amino acids, the MARTINI force field was developed by Marrink and coworkers [12] to develop a general coarse-grained model for all bio-macromolecules with as few bead types as possible. Each kind of amino acids was represented by one bead type as shown in

Figure 3, assigned with different interaction strengths. Only such four interaction types as polar, nonpolar, apolar and charged are created in this force field with 5 level of interaction strength of each type.

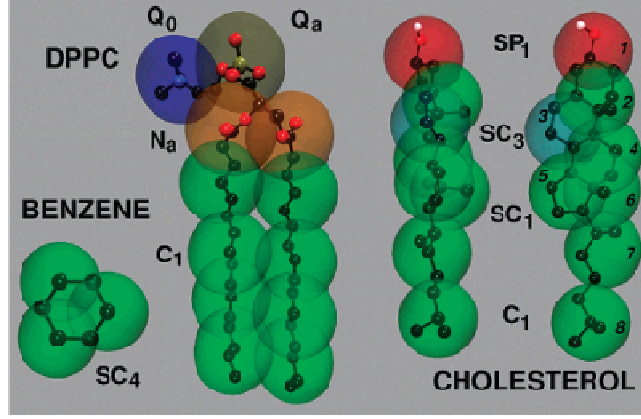


Figure 3. Mapping between the chemical structure and the coarse grained model for DPPC, cholesterol, and benzene using MARTINI approach [11]

The expression of MARTINI force field is shown as below as described by Marrink [12]:

$$\begin{aligned}
 E_{\text{MARTINI}} &= E_{\text{bonded}} + E_{\text{angle}} + E_{\text{nonbonded}} + E_{\text{el}} \\
 &= \sum V_{\text{bond}}(R) + \sum V_{\text{angle}}(\theta) + \sum U_{\text{LJ}}(r) + \sum U_{\text{el}}(r)
 \end{aligned}
 \tag{Eqn. 6}$$

where bonded and angle potentials are both in harmonic form:

$$V_{\text{bond}}(R) = \frac{1}{2} k_{\text{bond}} (R - R_{\text{bond}})^2
 \tag{Eqn. 7}$$

$$V_{\text{angle}}(\theta) = \frac{1}{2} K_{\text{angle}} (\cos \theta - \cos \theta_0)^2
 \tag{Eqn. 8}$$

The expression of nonbonded interactions is Lennard-Jones between interaction sites i and j :

$$U_{\text{LJ}}(r) = 4\epsilon_{ij} \left[\left(\frac{\sigma_{ij}}{r} \right)^{12} - \left(\frac{\sigma_{ij}}{r} \right)^6 \right]
 \tag{Eqn. 9}$$

If there are charged groups, a shifted Coulombic potential energy function with relative dielectric constant $\epsilon_{ij} = 15$ is applied to the system:

$$U_{\text{el}}(r) = \frac{q_i q_j}{4\pi\epsilon_0\epsilon_r r} \quad (\text{Eqn. 10})$$

The simplicity and versatility of the parameterization for different biomolecules are main advantages of MARTINI force field while its obvious disadvantage is the restriction of coarse-graining scale, resulting a still limited time and length scale and ineffective computation.

1.3.4. Bottom-up method for setting up theoretical framework

Since the biological function of a macromolecule is determined by its structure, an excellent coarse-graining method should catch the main characteristic structure of biomolecules rather than detailed chemical nature. If you want to set up your own coarse-grained potentials for your model, firstly you should have a clear understanding about relationships of each coarse-grained group. The consideration aspects range from non-bond potential, bond potential, angle potential, dihedral potential, improper potential to electrostatics. The harmonic expression are the simplest mode for intra-molecule potentials, LJ and any transformation of LJ potential are good choices for non-bond interactions. The electrostatics can be described by Coulombic potential function. Sometimes other potentials are included for specific molecules, for example, the stacking energy should be considered for DNA.

1.4. Model formulation of coarse-graining method

Even for the same system, the coarse-graining methods and procedures may be different according to the studied phenomenon of the system. Careful consideration must be taken ahead about what phenomenon would be studied and the coarse-graining scale of the system.

A universal step-by-step coarse-graining procedure doesn't exist, but the following factors are indispensable in a general coarse-graining framework:

1. Coarse-grained topological model mapped from all-atom biomolecule structure.
2. Potentials chosen to define and characterize the behavior of molecules.
3. Obtain potential parameters for coarse-grained model from all-atom model.
4. Benchmark case for validating the coarse-grained model with all-atom simulation or experimental results.

1.4.1. Set up the coarse-grained topological model

Two major approaches for setting up coarse-grained models are residue-based coarse-graining [13] and shape-based coarse-graining. Their mapping principles can be clearly introduced by their names. CG builder, a plugin in VMD package, is very effective for setting up coarse-grained topological model. Sometimes the combination of residue-based and shape-based coarse-graining approaches is considered for particular complex structures.

1.4.2. Characterize potentials for the system

In the coarse-grained model, it is aimed to use the fewest and simplest— but complex enough— potentials to represent the system structure, mechanical properties and interactions. After building up the coarse-grained topological model for the system, the necessary potentials to characterize the system should be determined.

In general, the total energy of a coarse-grained system is the sum of all utilized potentials:

$$E_{\text{system}} = E_{\text{CG}} = \sum \phi_{\text{CG}} \quad (\text{Eqn. 11})$$

To describe the total energy, firstly how many kinds of potentials should be applied needs to be determined; thereafter, the energy function for each potential will be defined.

1.4.3. Obtain potential parameters from all-atom models

After the coarse-graining potentials for the system are chosen, potential parameters such as k_i , r_0 , θ_0 need to be given. For a given structure, Energy Minimization [14] is performed with the all-atomistic simulation. After the system reaches the equilibrium state, coarse-grained potential parameters can be extracted from the energy function of all-atomistic simulation [15]. Energy Minimization is especially suitable for obtaining non-bonded potential parameters. The parameterization of coarse-grained bond strength can be determined by uniaxial stretching. A three-point bending test can be utilized to extract the bending stiffness of a molecule. The number of required tests depends on the number of coarse-grained potentials implemented to describe the system.

1.4.4. Validation of coarse-grained models

Once the coarse-graining potentials and parameters are fully-developed, the validation of coarse-grained model is necessary to assure an accurate representation. Two common validation approaches for validation are comparing results got from coarse-grained model with that from all-atomistic simulation or experimental results. Sometimes the comparison to all-atom simulation and to experimental results will be combined to verify the reasonability of coarse-grained system.

1.5. Algorithm flowchart for the coarse-grained molecular dynamics

A simplified description of the molecular dynamics simulation algorithm is depicted in Figure 4. The simulation proceeds iteratively by alternatively calculating forces and solving

the equations of motion based on the accelerations obtained from the new forces. Practically, almost all MD codes use much more complicated versions of the algorithm, including two steps (predictor and corrector) in solving the equations of motion and many additional steps for e.g. temperature and pressure control, analysis and output.

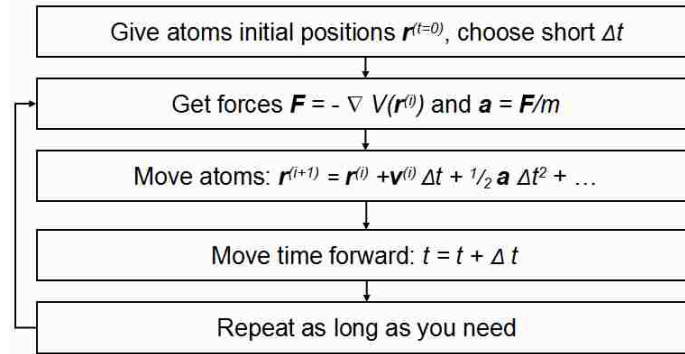


Figure 4. Algorithm flowchart for Coarse-Grained Molecular Dynamics

2. Biomarker Binding on an Antibody-Functionalized Biosensor Surface

Antibodies have been used as bioreceptors in bio-diagnostic devices for decades, whose performances are affected by various factors such as orientation, density, and local environment. While there are extensive works on designing and fabrication of various biosensors, little is known about the molecular level interactions between antibodies coated on sensor surfaces and biomarkers suspended in medium. In this paper, a coarse-grained model for biomarkers binding on an antibody-functionalized biosensor surface is constructed to study effects of surface properties and external parameters on antibody orientation and biomarkers binding time. The surface interaction type is found to significantly influence the antibody orientation and biomarker binding time. A proper electric field range is discovered to not only well-orientate antibodies but also steer biomarkers toward the surface, consequently reducing the binding time of biomarkers by two orders of magnitude. Moreover, a suitable surface coating density of antibodies has been proposed to help antibody orientation as well as biomarker binding. These findings can be used for rational design of biosensors with higher efficiency and more sensitive detections.

2.1. Introduction

Biosensors are effective tools for early diagnosis of diseases and biochemistry analysis.[16] After several decades of efforts, current biosensors have become more miniaturized, portable, effective and sensitive than before. Despite the significant progress achieved in biosensor developments, the molecular-level understanding of the biomarker binding process is still limited, which has hindered the further improvements of biosensors.

Various techniques such as electrical, mechanical, magnetic and optical approaches, have been applied to achieve better performance of biosensors.[17] Electric field has been widely used as an assistant in biosensor design by improving the selection efficiency.[17] The effects of electrostatic interactions on the association process of monoclonal antibodies (Abs) have been studied and compared with experimental results[17, 18]. The ionic concentration[19] and dipole moment of Abs[20] which would cause electrostatic forces have been claimed to be able to control the orientation of adsorbed Abs. It has also been verified[21] that the affinity and orientation of Abs under the dominance of electrostatic forces are different from those under the dominance of van der Waals interactions. Although the significance of electrostatic effects has been demonstrated[21-24] by researchers from different aspects, its effects on motion of biomolecules are not yet fully understood. To reveal the binding process of biomarkers-Abs[25-29] and explore possible contributions of electrokinetics on biosensing, a multiphysics computational model at the molecular level is needed.

The surface density of Abs is another important factor in the biomarker binding process. The monolayer coverage has been experimentally verified to considerably influence the Abs orientation[30-32]. With a reasonable high surface density, Abs are more feasible to capture biomarkers[33]. However, it is also observed that extremely high surface density may screen each other from binding targets. For example, it is found that Abs are more likely to congregate with each other, which is harmful for Abs-antigen binding, at extremely high concentrations.[34, 35] Therefore, an optimal surface density of Abs should be chosen to achieve the best possible biosensing performance, which calls for a clear understanding of effects of Abs surface coating density on Abs orientation and biomarker binding efficiency.

It has also been proven that Ab orientations can be controlled by surface properties[36-38], thus a lot of studies have been carried out on the correlation between surface properties and performances of Abs under different immobilization methods[34][35].

This paper aims to develop a multiphysics model to understand the biomarkers binding process on Ab-coated surface at the molecular level. Usually, Molecular dynamics (MD) is used to capture the detailed dynamics of biomolecules interactions. Given the length (micrometers or bigger) and the time scale (microseconds or longer) of our system, pure MD simulations are not feasible because the atomistic molecular dynamics modeling is limited to simulations on the nanometer and nanosecond scale. Thus, a coarse-grained (CG) MD[39] method is proposed to model the interaction of Abs-functionalized surface with biomarkers because it not only accesses this time and length scale, but also reduces the computational cost[40].

2.2. Methods

2.2.1. CG topology

The CG biosensing system was constructed as a self-assembled monolayer (SAM) coated on Si substrate in a field effect transistor (FET) based biosensor, similar to that in Tian *et al.* [41]. While bio-FET was chosen as a typical biosensor in this work, it should be noted that this study of biomarkers binding could be applicable to all kinds of Abs-functionalized sensors.

The substrate with a size of $50 \text{ nm} \times 50 \text{ nm}$ was made up of 1824 CG Si[42] beads. Each of CG Si beads was mapped from 121 all-atom Si atoms. Alkanethiols were chosen as the SAM molecules, each of which consisted of an alkyl chain as the tail group, a $(-\text{C}-\text{C}-)_n$

chain as the back bone and a S-H chain as the head group[43]. In the coarse-graining process, each alkyl chain was mapped into one bead that was attractive to the substrate; each $(-C-C)_6$ group was mapped into one bead which was neutral to other molecules; besides, the S-H groups were mapped into another kind of beads which attached to Abs tightly[23]. The SAM length can be adjusted by changing the number of neutral beads.

Immunoglobulin Gs (IgGs) were used as bioreceptors due to their innate high specificity and versatility[9, 44-50] in biosensor design. The IgG contains two light and two heavy chains which are linked by disulfide bonds[34]. As shown in Figure 1 (a), each heavy chain is constructed by three constant domains denoted as C_{H1} , C_{H2} and C_{H3} , and a variable domain as V_H ; on the other hand, each light chain consists of one constant domain C_L and one variable domain V_L . Consequently, most of CG models of Abs are formed as a characteristic Y-shaped configuration[51] with 12 parts. The CG model of IgG1 was built up referring to the 12-bead colloidal model of Abs created by Zhou *et al.*[52] and the Elastic Network Normal-Mode analysis constructed by Chaudhri *et al.*[34, 35]. The all-atom model of the IgG1 molecule was downloaded from the RCSB data bank and was mapped into a 12-bead CG model in which each bead represented one domain. The CG Ab model was treated as symmetric, as shown in Figure 5 (b). The total charge of the CG Ab model was neutral but it had dipole moment due to its non-uniform internal charge distribution. The dipole moment of Abs was calculated by the Protein Dipole Moment server[34]. The mass, charge and indicated domain of each bead are shown in Table 1.

Furthermore, other topological information such as atom types, bonds, angles and dihedrals are plotted in Figure 5.

Table 1. Information of each bead in the CG Ab model

Atoms	Mass	Charge (eV)	Indicated domains
1,2	12530	-1	C _{H3}
3,4	11936	0	C _{H2}
5,9	11030	0	C _L
6, 10	13724	0.5	V _L
7, 11	11908	0.5	V _H
8, 12	10141	0	C _{H1}

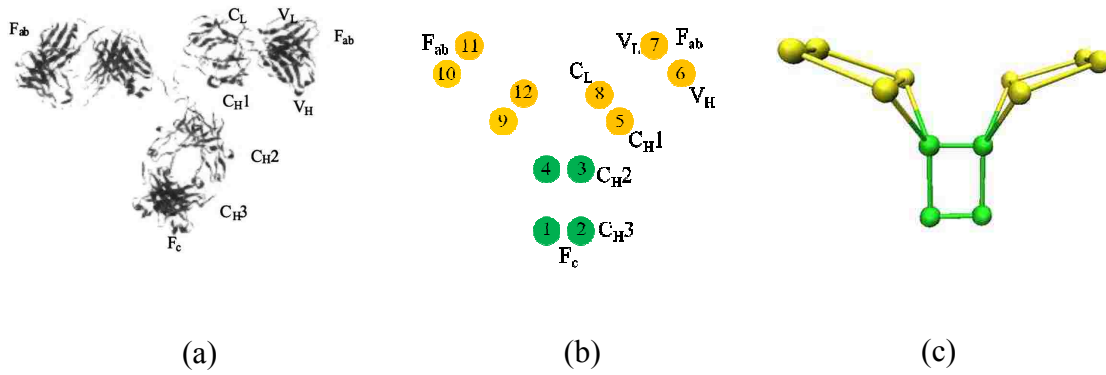


Figure 5. (a) All-atom model of Ab[26]; (b) Detailed topological information of CG Ab model (12 atoms, 4 atom types; 16 bonds, 5 bond types; 16 angles, 5 angle types; 5 dihedrals, 5 dihedral types.); It should be noted that atoms with the same color don't mean they are the same atom type. (c) CG model of Abs.

Following the same coarse-graining method, the all-atom model of the biomarker[53] was mapped into an arrow-shaped CG model using the residue-based CG method, as shown in Figure 6. Four strong binding sites were placed on the head of the biomarker while two weak binding sites were located on its tail.

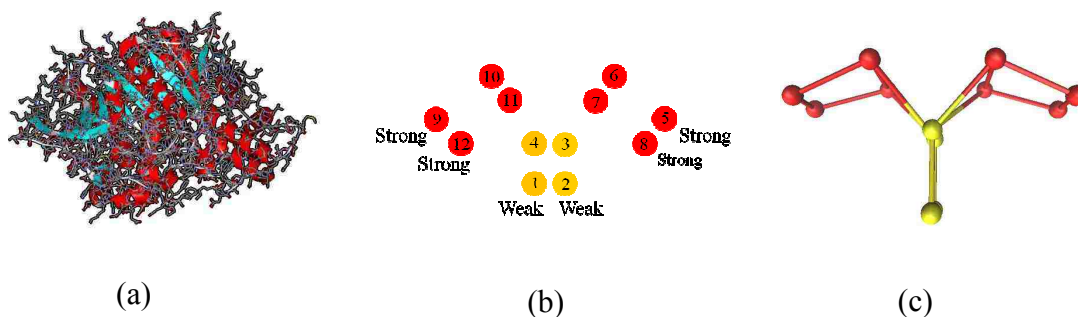


Figure 6. (a) All-atom model of biomarker[53]; (b) Detailed topological information of CG biomarkers (12 atoms, 4 atom types; 14 bonds, 5 bond types; 16 angles, 5 angle types; 5 dihedrals, 5 dihedral types). It should be noted that atoms with the same color don't mean they are the same atom type. (c) CG model of biomarkers

After Abs were immobilized on the substrate surface by SAMs, biomarkers were released from a height of 10 nm above Abs. The established CG system for biomarkers binding on Abs-functionalized surface is shown in Figure 7. It should be noted that the density of SAMs is usually 100 times higher than that of Abs in real situation. However, modeling all free SAMs was not necessary and would dramatically increase the computational cost in our simulations. Thus, only those SAMs connected with Abs were modeled. The motion of each SAM was constrained in a certain zone which was calculated out according to the surface coating density of SAMs.

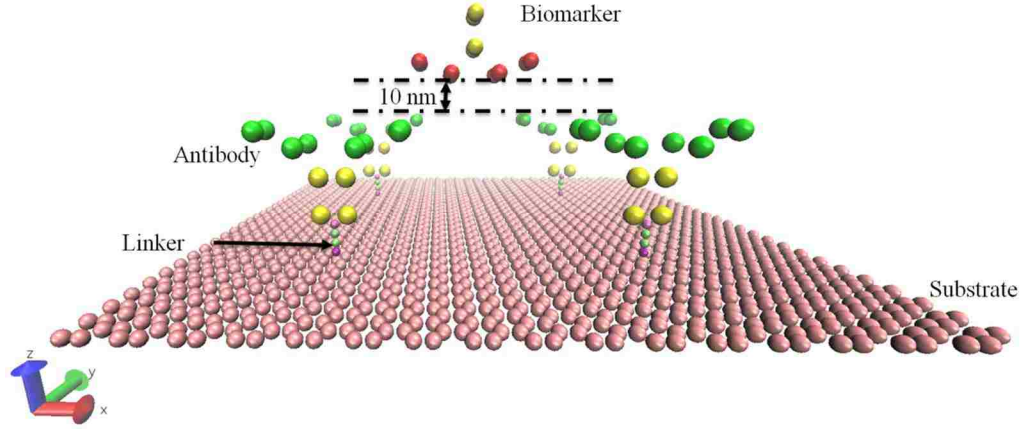


Figure 7. Simulation system setup. Four Abs are immobilized on the substrate by SAMs, one biomarker is released from a height of 10 nm above Abs.

2.2.2. CG potentials

The coarse-grained force field is the sum of inter-molecular and intra-molecular interactions, which can be written as:

$$U_{total} = U_{inter} + U_{intra} \quad (\text{Eqn. 12})$$

The inter-molecular interactions consist of electrostatic and van der Waals interactions[35]. The electrostatic interaction is expressed in Debye form while the van Der Waals is represented by Lennard-Jones (LJ) potential:

$$U_{inter} = U_{coul} + U_{lj} = \frac{q_i q_j}{4\pi\epsilon_r r} \exp(-\kappa r) + 4\epsilon_{ij} \left[\left(\frac{\sigma_{ij}}{r} \right)^{12} - \left(\frac{\sigma_{ij}}{r} \right)^6 \right] \quad (\text{Eqn. 13})$$

Where q_i and q_j represent the net charges on CG sites, ϵ_r indicates the effective dielectric constant while κ is the Debye screening parameter. ϵ_{ij} is the well depth for ij th pair of CG sites and σ_{ij} is the finite distance at which the inter-particle potential for ij th pair is zero. Determining the value of dielectric constant for protein solutions has been challenging researchers for long[54]. Though a lot of work[53-56] has been done on evaluating the

effective dielectric constant in the presence of explicit/implicit water, no consensus has been reached on how to calculate it within and between two protein molecules[57, 58]. In current study, the values for proteins and solvent are just fixed at the same with that of Chaudhri *et al.*[34]. The exact value of the effective dielectric constant will be studied along with flexible proteins models in future.

The bond, angle and dihedral potentials constitute the intra-molecular interaction, all of which are defined based on harmonic approximations of interaction strengths:

$$U_{intra} = U_{bond} + U_{angle} + U_{dihedral} = \kappa_{bond}(r - r_0)^2 + \kappa_{angle}(\theta - \theta_0)^2 + \kappa_{UB}(r - r_{UB})^2 + \kappa_{dihedral}[1 + \cos(\varphi - d)] \quad (\text{Eqn. 14})$$

Here κ_{bond} , κ_{angle} , κ_{UB} , $\kappa_{dihedral}$ refer to the spring constants for bond, angle, Urey-Bradley (UB) and dihedral terms, respectively. r_0 , θ_0 , r_{UB} and d are equilibrium bond, angle, UB and dihedral terms respectively.

All of intra-molecule potential data for Abs were extracted from Ref. [34] while the rest were obtained by applying the Energy Minimization (EM) method[26]. The bond and angle potential parameters were determined following the work of Brandt *et al.*[59].

2.2.3. Validation of CG model

To ensure the CG model accurately described the molecular motion, a benchmark case was performed by comparing diffusion coefficients (Ds) of Abs and biomarkers obtained from CG MD results and all-atom results. At 293 K, Abs and biomarkers were released in a fluidic box with periodic boundaries. Their diffusion processes were simulated by both of all-atom MD and CG model. The effects of solvent were represented by the Langevin thermostat.

The D s of Abs and biomarkers were calculated by the simulation results. Based on Einstein’s theory, the displacement of a Brownian particle is proportional to the square root of the elapsed time.[60]

$$\langle |\mathbf{r}|^2 \rangle = 6Dt \quad (\text{Eqn. 15})$$

Where $\langle \rangle$ means the time average, \mathbf{r} is the position vector of Abs/biomarkers, t stands for time and D for the diffusion coefficient. Given \mathbf{r} and t , the diffusion coefficient can be calculated.

The D s of Abs and biomarkers, calculated from both all-atom model and CG model, are listed in Table 2. Referring to the measured value of Abs by Saltzman *et al.*[61], both all-atom and CG results for the Ab are within the suggested range, indicating good agreement with the experimental results. The D s of biomarkers from two models were also similar, and agrees with the clinical data.[62] This benchmark case illustrated that our CG system have captured the essential diffusion motion of Abs and biomarkers.

Table 2. Diffusion coefficients calculated from two models

Diffusion coefficient	Ab (10^{-7} cm ² /s)		Biomarker (10^{-5} cm ² /s)	
	Calculated value	Cited value[61]	Calculated value	Cited value[62]
All-atom model	4.421	4.4 ± 1.3	2.101	2.06
Coarse-grained model	4.852	—	2.319	—

Our coarse-grained model can also be validated by comparing the calculated Gibbs free energy (ΔG) differences of antibody-biomarker complexes. Following the work of Novotny *et al.*[63], ΔG of antibody-biomarker complex has been calculated based on both full-atomistic and coarse-grained models. ΔG of antibody-biomarker complex formation in

the coarse-grained model was -11.0 kcal while it was -6.8 kcal in the full-atomistic model. Overall, the ΔG difference of 4.2 kcal between the two models was within the acceptable range (difference in the range of -9 ± 3 kcal [63] is reported in Novotny's work. From this result, our coarse-grained model underestimated the strength of antibody-biomarker complex. This underestimation will be studied in the future through further refinement in the coarse-grained model.

Orientation factor (a), is derived to describe the orientation of Abs, following a similar definition used by Zhou *et al.* [64]. In our model, the orientation factor is defined as the cosine value of the offsetting angle (θ) of Abs from the normal direction of the substrate surface, as shown in Figure 7. A larger a indicates a better orientation of Abs which represents a higher possibility of binding biomarkers.

The CG MD simulation was run by the LAMMPS[65] package. The time step for the simulation was 0.01 ps. The simulation process was continued until one biomarker bound with Abs. The temperature of the system was 293 K. The dielectric constant for the solution was 20.0 while it was 1.0 for biomolecules[34]. The NVE integration was applied to the system with Langevin dynamics representing the Brownian motion of fluid. Molecules interacted with each other by van der Waals and Coulombic forces. Hydrophobic effects of solvent to rigid CG structures of Abs and biomarkers have been excluded[34] because the solvent is not a necessity in coarse-grained molecular dynamics simulations[66].

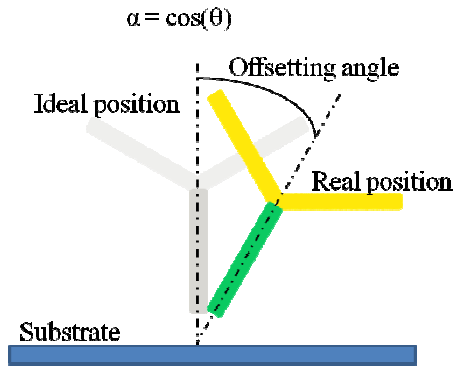


Figure 8. Schematic of Ab orientation factor. θ varies from 0° to 90° while α is constrained in the range of $[0,1]$. When the Ab is perpendicular to the substrate surface, α is equal to 1 which is best for biomarker binding; when the Ab lies flat on the substrate surface, α is equal to 0 which is not beneficial for biomarker binding.

2.3. Results and Discussions

The binding processes of biomarkers under different physical conditions were simulated with the developed CG MD model. A typical Ab-biomarker binding process is shown in Figure 9.

interaction type is defined as neutral, the surface neither attracts nor repels them. Different interaction types are achieved by adjusting the sigma (σ), epsilon (ϵ) and cutoff distance (r_c) of LJ potentials between the substrate and other molecules. Potential parameters of the substrate under different surface interaction types are listed in Table 3.

Table 3. Potential parameters between the substrate and other molecules

Interaction	σ (Å)	ϵ	r_c (Å)
Strong	6.8	1	20.4
Weak	6.8	0.5	20.4
Neutral	6.8	0	6.8
Weak	6.8	0.5	6.8
Strong	6.8	1	6.8

The SAM length was set as 0.8 nm while the surface coating density was fixed at $1600/\mu\text{m}^2$ in this set of simulations. As shown in Figure 10 (a), orientation factors of Abs varies from 0.58 to 0.87 if no electric field is applied. When the interaction between the substrate and biomolecules is set as strong attraction, most of Abs are found to be tightly laid on the surface, referred to the “side-on” as mentioned[60]. When a weak attraction is applied, Abs can easily detach from the substrate after absorption, different from the strong attachment observed under strong attractions. The neutral interaction was applied by setting ϵ between the substrate and other molecules as zero along with a reflection wall on the surface of the substrate. Moving molecules would bounce back once they contact the reflection wall. When the surface interaction type is neutral, Abs oscillate around 30° with vertical axis, resulting in an orientation factor around 0.73. On the other hand, when the interaction is repulsive, the orientation factor is above 0.85, implying that the repulsive interaction is more beneficial for the Abs orientations than the neutral or attractive

interaction states. With an electric field applied, the orientation factors can be kept above 0.90, under any interaction types.

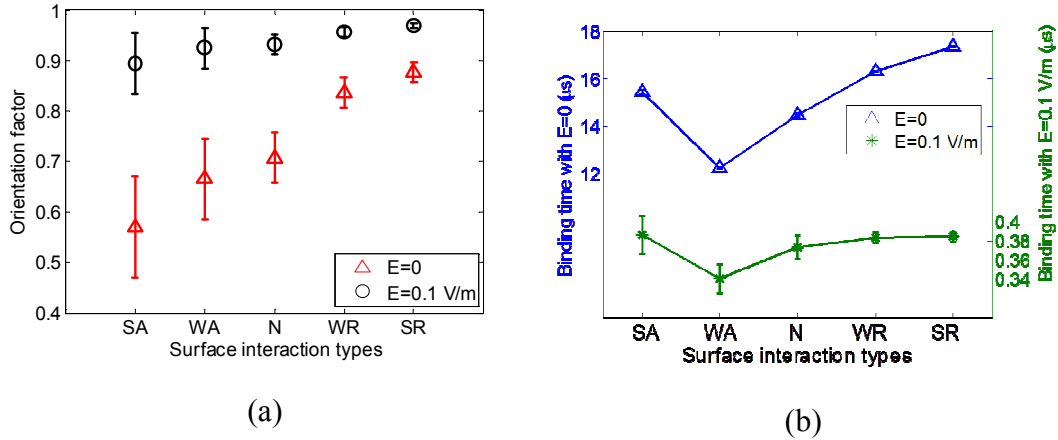


Figure 10. (a) Orientation factors under different surface interaction types: SA - strong attraction, WA - weak attraction, N - neutral, WR - weak repulsion, and SR - strong repulsion. (b) Biomarkers binding time under different surface interaction types.

The effects of surface interaction type on the biomarkers binding time are more complicated than those on Abs orientation because the surface interaction type not only affects the behavior of Abs but also impacts the motion of biomarkers. From Figure 10 (b), the weak attraction is demonstrated to be most efficient for biomarkers binding. Without an electric field, the biomarker binding time is 12.67 μs under the weak attraction, while it is larger than 14.50 μs under any other interaction types. A strong attraction may trap Abs onto the surface permanently, and decrease the chance of binding Abs which would not happen under weak attractions. The repulsive substrate offers better orientation conditions for Abs, but also repels biomarkers away when they are close to the surface. According to these results, the weak attraction is the most effective interaction type for the binding of biomarkers. The same trend is also observed when an electric field is utilized, where the

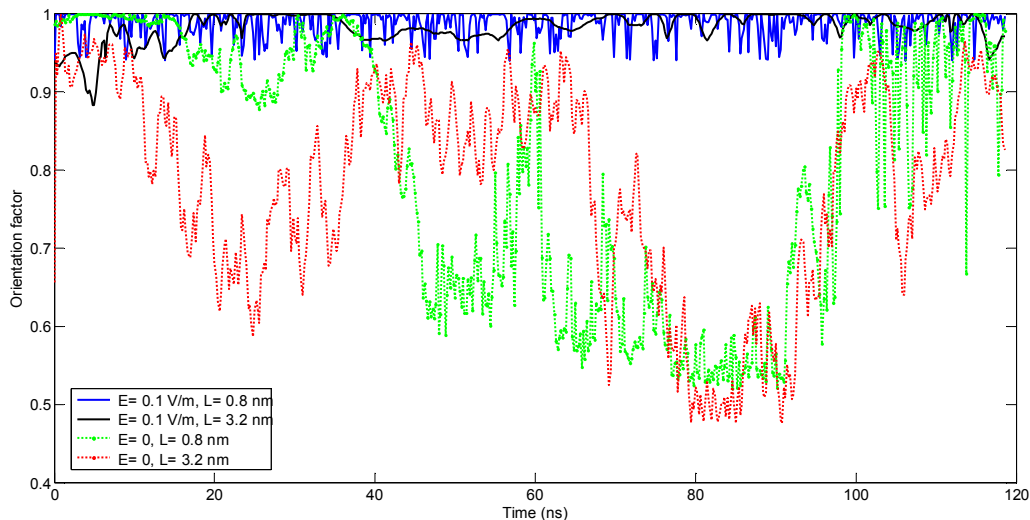
binding time with weak attractive substrate is the smallest among those five substrate interaction types.

Based on the fact that the weak attraction between the substrate and biomolecules helps the binding process of biomarkers most, the following results are all obtained from a weak attractive substrate. In future, the detailed study of hydrophobic effects will be included in a more precise model with flexible protein structures.

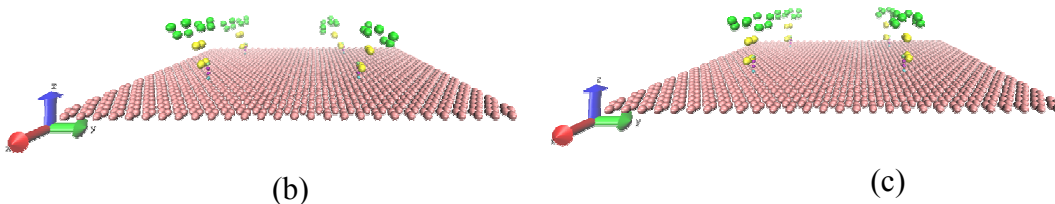
2.3.2. Effects of electric field strength

To better understand how an electric field influences Abs orientation and biomarkers binding efficiency, electric field with different strengths were applied to the system. The value of the electric field strength was set as 0, 0.01, 0.05, 0.1 and 0.2 V/m according to the typical range used in biosensors[61, 62]. A higher value of 0.5 V/m beyond the normal range was also included for comparison purposes. This set of simulations were carried out under the surface coating density of $1600/\mu\text{m}^2$ and the SAM length of 0.8 and 3.2 nm, respectively.

Figure 11 demonstrates how the electric field affects the orientation of Abs. The time histories of Ab orientation factors under various conditions are plotted in Figure 11 (a). Abs fluctuate locally with large angles when there is no electric field. With an electric field, the offsetting angles of Abs can be controlled within 20° , which indicates that the orientations of Abs are well constrained. Figure 11 (b) and (c) are schematics of Ab orientations under different electric field conditions. It is shown that Abs may bend and tilt without an electric field, while they are well-orientated and able to bind biomarkers faster under an electric field.



(a)



(b)

(c)

Figure 11. (a) Time history of Abs orientation factors under different conditions. The blue solid line is the time history of Ab orientation factors with an electric field strength of 0.1 V/m and SAM length of 0.8 nm; the black solid line is the time history of Ab orientation factors with an electric field strength of 0.1 V/m and SAM length of 3.2 nm; the red dashed line is the time history of Ab orientation factors without an electric field and SAM length of 0.8 nm; the green dashed line is time history of Ab orientation factors without an electric field and SAM length of 3.2 nm. (b) A typical snap shot of Abs orientation without an electric field. (c) A typical snap shot of Abs orientation with an electric field.

The variation of Ab orientation factors under different electric field strengths and SAM lengths are shown in Figure 12 (a). The electric field has little impact on Abs orientations if its strength is smaller than 0.05 V/m; however, when it increases from 0.05 V/m to 0.2 V/m, the Ab orientation factor will increase dramatically; after its strength goes

above 0.2 V/m, further rising of the electric field strength will no longer influence the orientation of Abs apparently. It is also shown that shorter SAMs are more beneficial for Abs orientations because a longer SAM will make the Abs more prone to fluctuations. However, the influence of SAM length on Abs orientation is much less dominant compared to that of electric field.

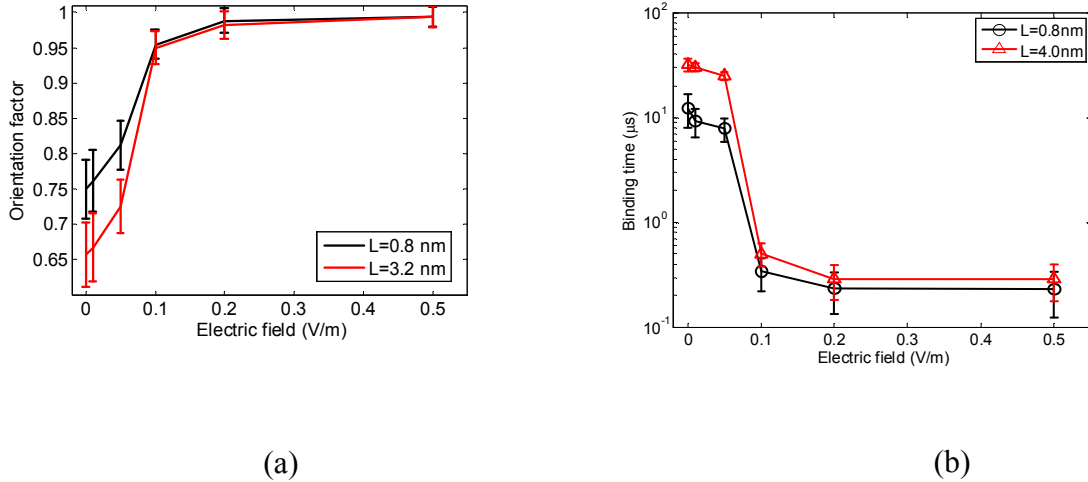


Figure 12. (a) Abs orientations under different electric field strengths and different SAM lengths. (b) Biomarker binding times under different electric field strengths and different SAM lengths.

Effects of the electric field on biomarkers binding time are shown in Figure 12 (b). The application of an electric field is shown to reduce the biomarker binding time by two orders of magnitude, from μs to ns. The biomarker binding time varies from 10 μs to 100 μs without an electric field, while it is less than one μs with an electric field strength of 0.1 V/m. Moreover, the correlation between electric field strengths and biomarkers binding time is nonlinear. When the field strength is smaller than 0.05 V/m, the electric field is weak and consequently has little impact on the biomarker binding time. Field strengths exceeding 0.05 V/m lead to a dramatic reduction in binding time; however, further increase of the electric field strength above 0.2 V/m will no longer reduce the binding time apparently.

2.3.3. Effects of surface coating density

The vital role of surface coating density in biosensor efficiency has been verified by many experimental studies[26, 68-70], while our aim is to get a better understanding of the quantitative relationship between the coating density and biomarkers binding time. The coating density is adjusted by changing the number of Abs that are uniformly distributed per square micron on the substrate surface. In this set of simulations, the surface coating densities were selected as $100/\mu\text{m}^2$, $625/\mu\text{m}^2$, $1111/\mu\text{m}^2$, $1600/\mu\text{m}^2$, $3086/\mu\text{m}^2$ and $6400/\mu\text{m}^2$, with an electric field strength fixed at 0.1 V/m and a constant SAM length of 0.8 nm. The effects of coating density on Ab orientation factors and biomarker binding times are illustrated in Figure 13.

The surface coating density affects the orientation of Abs nonlinearly. As shown in Figure 13 (a), a higher surface coating density is more helpful for Abs orientation. When the surface coating density of Abs is $6400/\mu\text{m}^2$, under which condition Abs have covered the whole surface without overlapping, the Abs orientation factor is maintained at 0.97 even without an electric field. With smaller surface coating density, Abs have more free space to move which results in a larger variation in orientations. When the surface coating density is smaller than $2000/\mu\text{m}^2$, the Abs orientation factor decreases almost linearly with the coating density. For extremely small surface coating densities without an electric field, the Ab orientation factor can decrease to 0.72. However, with the assistance of an electric field, the Abs orientation factor can be controlled above 0.94 no matter how small the coating density is.

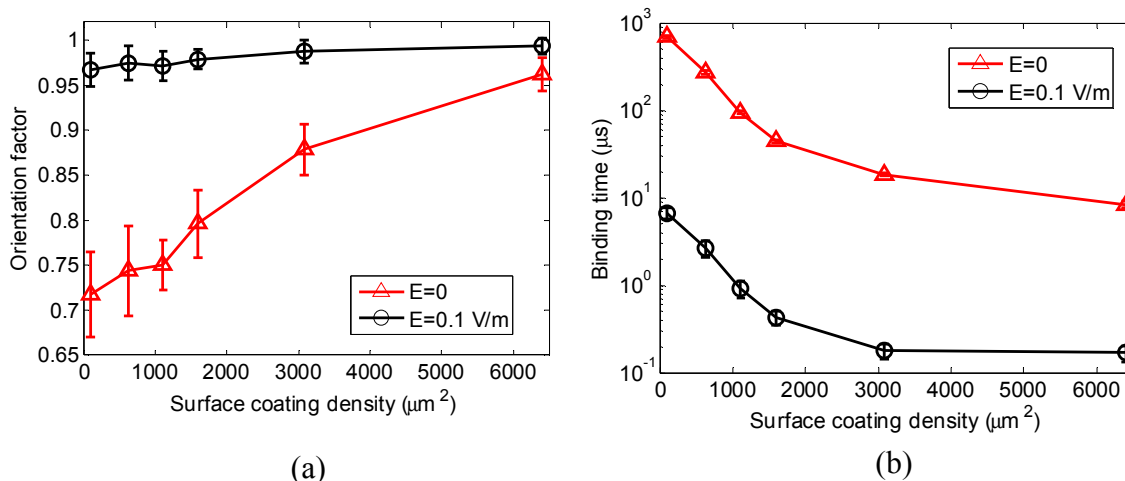


Figure 13. (a) Effects of surface coating density on Abs orientation factor. (b) Effects of surface coating density on biomarkers binding time.

Figure 13 (b) illustrates that the surface coating density can largely decrease the binding time of biomarkers: increasing the surface coating density from $100/\mu\text{m}^2$ to $6400/\mu\text{m}^2$ can reduce the biomarker binding time from ms to μs even without an electric field; a higher surface coating density leads to a shorter binding process of biomarkers. It should be noted that these results are obtained under the situation where Abs are never dense enough to block each other. If the surface coating density is so high that Abs are blocked by each other, the binding capabilities of this surface would be reduced. Under this condition, a higher surface coating density is not beneficial for the binding of biomarkers any more. But this strategy is still widely used in the biosensor application because it can prevent Abs from being washed away by the fluidic flow.

2.4. Conclusions

A CG MD model has been developed to study effects of surface interaction type, electric field strength, and surface coating density on biomarkers binding process. The CG multiphysics computational model has been validated by the fact that CG model results were

consistent with full-atomistic results when simulating the diffusion process of Abs and biomarkers in the stationary fluid. It should be noted that this is an initial study without testing the convergence of the model, a more refined model will be established in future investigations.

The surface interaction type can affect behaviors of both Abs and biomarkers. With the same physical condition settings, the strong repulsive substrate offers the best orientations for Abs while the strong attraction makes the orientations of Abs less favorable for biomarker bindings. However, the weak attraction between the substrate and other molecules is the most effective for the binding process when compared with the strong attraction, neutral, and repulsions.

Meanwhile, the electric field is capable of well-orientating Abs and guiding biomarkers toward the substrate, which consequently reduces the binding time and enhance the efficiency. The influence of the electric field is negligible when its strength is smaller than 0.05 V/m. A strength ranging from 0.05 V/m to 0.2 V/m, is found to dramatically reduce the binding time of near-surface biomarkers. Further ascending the electric field strength when it is already above 0.2 V/m will not cause extra decrease of the biomarker binding time noticeably.

Lastly, a higher surface coating density of Abs is favorable for the efficiency of the biosensor system. The binding time changes exponentially with the surface coating density and reduces nearly by two orders of magnitudes when the coating density increases from $100/\mu\text{m}^2$ to $6400/\mu\text{m}^2$. A denser surface coating can assure a satisfying orientation of Abs in comparison to sparser ones that don't affect the orientation of Abs at all.

In conclusion, weak substrate-biomolecule attraction, medium electric field strength, and high surface coating density are found to be most effective for fast biomarker binding. The results of this paper provide an understanding of biomarker binding process at molecular level and guidance to improve biosensor performance.

2.5. Acknowledgements

The authors acknowledge the supports for this work from National Science Foundation Grant Nos. CBET-1067502 and CBET-1113040 for Y.L., CBET-1064574 and ECCS-0955027 for W.H., and NSFC-91123023 for B. P..

3. Mechanical properties of nanoworm assembled by DNA and nanoparticle conjugates

Recently, DNA-nanoparticle conjugates have been widely used as building blocks for assembling complex nanostructures, due to their programmable recognitions, high cellular uptake and enhanced binding capabilities. In this study, a nanoworm structure, which can be applied in fields of drug targeting, image probing and thermal therapies, has been assembled by DNA-nanoparticle conjugates. Subsequently, its mechanical properties have been investigated due to their importance on the structural stability, transport and circulations of the nanoworm. Stiffness and strengths of the nanoworm under different deformation types are studied by coarse-grained molecular dynamics simulations. Effects of temperature, DNA coating density and particle size on mechanical properties of nanoworms are also thoroughly investigated. Results show that both resistance and strength of the nanoworm are the weakest along the axial direction, indicating it is more prone to be ruptured by a stretching force. In addition, DNA strands are found to be more important than nanoparticles in determining mechanical properties of the nanoworm. Moreover, both strength and resistance in regardless of directions are proved to be enhanced by decreasing the temperature, raising the DNA coating density and enlarging the particle size. This study is capable of serving as guidance for designing nanoworms with optimal mechanical strengths for applications.

3.1. Introduction

DNA[71-73] and nanoparticle (NP) conjugates[74] have been widely used as building blocks[75, 76] to construct complex one-, two- and three-dimensional structures[77-84] with

novel plasmonic[85-87], magnetic[76, 84, 88-90], luminescent[89, 91-93], catalytic[94-97], optical[98, 99], and electrical[100] properties. DNA-NP conjugates were firstly introduced by Mirkin *et al.*[101, 102] and then developed by many researchers to create structures at nano[103-106] and micro scale[107, 108]. The DNA-NP conjugate is mainly composed of the inorganic core and the DNA shell. The core acts as a scaffold for orientating DNAs into dense arrangements and provides physical and chemical properties to the structure. The DNA shell offers higher binding strengths, duplex stabilities[74, 84, 102], and enhanced cellular uptake without transfection agents[109]. Thus, the conjugate possesses multiple properties which have ensured its applications in fields of intracellular gene regulation[105, 110], molecular diagnostics[111-115], intracellular probe[116] and material synthesis[117-120]. When used as material synthesis blocks, one distinguishable advantage of DNA-NP conjugates is that their structural parameters such as NP diameter, shape, DNA length, and sequences can be tuned independently.

A nanoworm structure has been created by DNA-NP conjugates for its potential applications in fields of drug delivery[121, 122], image probing[123] and thermal therapy[124-126]. This chain-like structure is small enough to be influenced by Brownian forces yet large enough to be observed by ordinary light microscopy.[127] When applied under certain circumference[128, 129], it is required to have targeted delivering ability and a long enough circulating time in the blood flow[127]. Only with adequate mechanical strength, the nanoworm can avoid being ruptured by local flow stress, deliver drugs to infected regions effectively and improve the ability to target and image tumors[130]. Mechanical strengths of the nanoworm have been experimentally verified to be influenced by structural parameters such as the size and shape of NPs[131], DNA sequences and strand

lengths[132], coating density and the ratio of DNA length to NP diameter[133]. Gang *et al.* found that the stability of one dimensional structure is highly related to the interparticle distance and hybridized sequences between two particles[105]. Leventis *et al.* also observed that the strength of nanoworm can be obtained by choosing silicon or vanadia as colloid materials[134]. In addition, Biswal *et al.* investigated relationships of the stability of DNA-linked colloidal chains and the external magnetic field strength, DNA length and coating density[107]. However, a systematic relationship between mechanical properties of the nanoworm and structural parameters has yet to be studied. Our goal is to study effects of physical conditions and structural parameters on mechanical properties of the nanoworm to enhance their stability and transport ability.

Considering difficulties of experimentally measuring mechanical strength at molecular level[79, 132, 135-141], a Molecular Dynamics (MD) simulation model for DNA-NP interactions is developed. The most essential part for the model is to capture significant characteristics of DNA, such as the hybridization ability, melting transition, stiffness and binding strength. Thus, a proper DNA model is needed. Existing full-atomistic DNA models cannot access the required length and time scales of our system, due to large quantities of strands used in the structure. Therefore, a proper coarse-grained (CG) model with minimal number of degrees of freedom should be used to capture significant characteristics of DNA. Pablo *et al.* have developed a new 3 Site-Per-Nucleotide (3SPN)[130, 142, 143] CG model which retains important properties for DNAs. This model can be easily implanted into existing molecular dynamics packages LAMMPS[144]. So it is directly used in our system to represent behaviors of DNAs.

This paper aims to analyze the stiffness and strength of the nanoworm under different types of loadings with the developed CG MD model. Influences of the temperature, DNA coating density and particle size are also studied on mechanical properties of the nanoworm to achieve optimal designs of this structure.

3.2. Methods

A CG MD model is built up to examine detailed molecular interactions of nanoworm assembled by DNA-NP conjugates. DNA strands are represented by 3SPN2 model[145] while each NP is modeled as a single spherical particle[105] with specific diameters and masses. Total potential (U) for the system can be categorized into two sections: potentials involving NPs (U') and potentials purely for DNAs (U'').

U' includes interactions among NPs as well as those between NPs and DNAs. Non-bonded part for U' is mainly made up of repulsive forces among NPs and weak attractions between DNAs and NPs. The repulsive forces among NPs are expressed by a truncated Lennard-Jones (LJ) potential with a cutoff distance equal the sigma value.

$$\begin{aligned}
 U_{NP-NP} &= 4\varepsilon_{ij} \left[\left(\frac{\sigma_{ij}}{r} \right)^{12} - \left(\frac{\sigma_{ij}}{r} \right)^6 \right] & r < r_c, \\
 &= 0 & r \geq r_c \\
 & & r_c = \sigma_{ij}
 \end{aligned} \tag{Eqn. 16}$$

Where ε_{ij} is the well depth for ij_{th} pair of CG sites and σ_{ij} is the finite distance at which the inter-particle potential for ij_{th} pair is zero. It should be noted that this modeling method for NPs is only available when the ratio of NP diameter to DNA length (ζ_r) is relatively small (<5) because there is no direct contact between NPs due to the thickly and densely

packed DNA shell. As long as ζ_r is large enough to have direct contact between NPs, the contact potentials[146, 147] for NPs should be considered.

The weak attraction between NPs and DNA strands are described by LJ/cut potential with a cutoff distance equal 2.5 times of sigma value. Parameters for these potentials are obtained using Energy Minimization method[3, 148].

$$\begin{aligned}
 U_{DNA-NP} &= 4\epsilon_{ij} \left[\left(\frac{\sigma_{ij}}{r} \right)^{12} - \left(\frac{\sigma_{ij}}{r} \right)^6 \right] & r < r_c \\
 &= 0 & r \geq r_c \\
 & & r_c = 2.5\sigma_{ij}
 \end{aligned} \tag{Eqn. 17}$$

DNA strands are connected to NPs by fixing ends of each strand onto the surface of NP, so no bonded interaction exists in the NP-NP and NP-DNA section. Therefore, potentials involving NPs (U') can be summarized as

$$U' = U'_{nb} = U_{DNA-NP} + U_{NP-NP} \tag{Eqn. 18}$$

Potentials purely for DNAs (U'') are made up of non-boned part (U''_{nb}) and bonded section (U''_b). The non-bonded potential for DNA (U''_{nb}) is can be summed as[145]

$$U''_{nb} = U_{exe} + U_{bstk} + U_{cstk} + U_{bp} + U_{elec} \tag{Eqn. 19}$$

Where U_{exe} , U_{bstk} , U_{cstk} , U_{bp} and U_{elec} denote excluded volume effects, intra-strand base stacking, inter-strand cross-stacking, base pairing interactions and screened electrostatic for DNA strands, respectively.

The bonded potentials for DNA (U''_b) are made up by bond, angle, and dihedral sections,

$$U''_b = U_{bond} + U_{bend} + U_{tors} \tag{Eqn. 20}$$

where bond potentials (U_{bond}) are harmonic and anharmonic, angle section (U_{bend}) is harmonic and the dihedral contribution (U_{tors}) is given by a Gaussian well. Detailed introductions of each term are described as[145]

$$U_{bond} = \sum_i^{bonds} k_b (r_i - r_{0,i})^2 + 100k_b (r_i - r_{0,i})^4 \quad (\text{Eqn. 21})$$

$$U_{bend} = \sum_i^{bonds} k_\theta (\theta_i - \theta_{0,i})^2 \quad (\text{Eqn. 22})$$

$$U_{tor} = \sum_i^{dihedrals} -k_\phi \exp\left(\frac{-(\phi_i - \phi_{0,i})^2}{2\sigma_{\phi,i}^2}\right) \quad (\text{Eqn. 23})$$

Where k_b and $r_{0,i}$ are the force constant and equilibrium bond length for bond i ; k_θ and $\theta_{0,i}$ represent the force constant and equilibrium angle for angle i ; k_ϕ , $\phi_{0,i}$ and $\sigma_{\phi,i}$ denote the well-depth, equilibrium angle and Gaussian well-width of dihedral i , respectively.

After established CG force field for the system, topologies for the model should be developed. The first step is to design the coating DNA strand. Referring to Figure 14 (a), the coating DNA consists of three parts: a spacer section which is a single strand with 10 Thymines (Ts), a bridging section that is the double strand with Cytosine-Guanine (C-G) pairs and a linker which is a single strand. The linker has palindromic sequences[149], so it can form interparticle-linkages by hybridizing with other linkers on adjacent NPs. After the coating DNA strand is designed, the DNA-NP conjugate is assembled with specific structural parameters. The model for an assembled DNA-NP conjugate is shown in Figure 14 (b), followed by a nanoworm constructed by conjugates in Figure 14 (c).

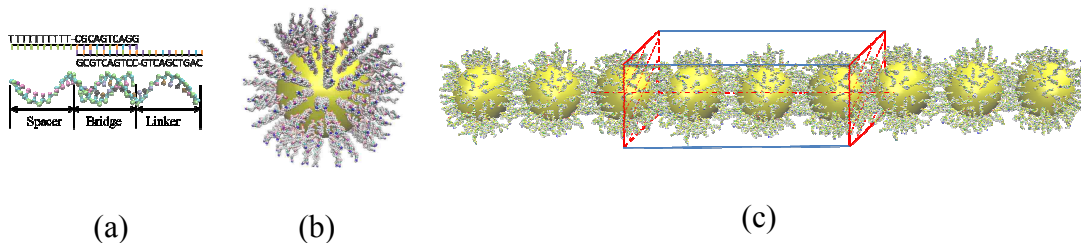


Figure 14. CG topological models for (a) coating DNA, (b) DNA-NP conjugate and (c) the nanoworm constructed by conjugates

Two benchmark cases have been performed to validate the CG MD model of DNA-NP conjugates from both mechanical and structural aspects. In the first case, mechanical properties of DNA strands are tested by tensile load following the work of Piana *et al.*[150], as shown in Figure 15 (a). Physical settings for the tensile test of DNA strands, energy/force-extension curves of our model and those of Piana *et al.*[150] are demonstrated in Figure 15 (a) (I), (II) and (III), respectively. The energy/force-extension curves obtained from our model has been found to agree well with results reported in Ref.[150], indicating our model has sustained fundamental mechanical properties of DNA strands. In the second case, the internal structure of dimers assembled by DNA-NP conjugates is also studied and compared to results of Gang *et al.*[151], as shown in Figure 15 (b). It is clear that the relationship between the inter-displacement of NPs (D_n) and the length of coating DNAs (represented by numbers of DNA bases) in our dimer agrees well with that of Gang *et al.*[151].

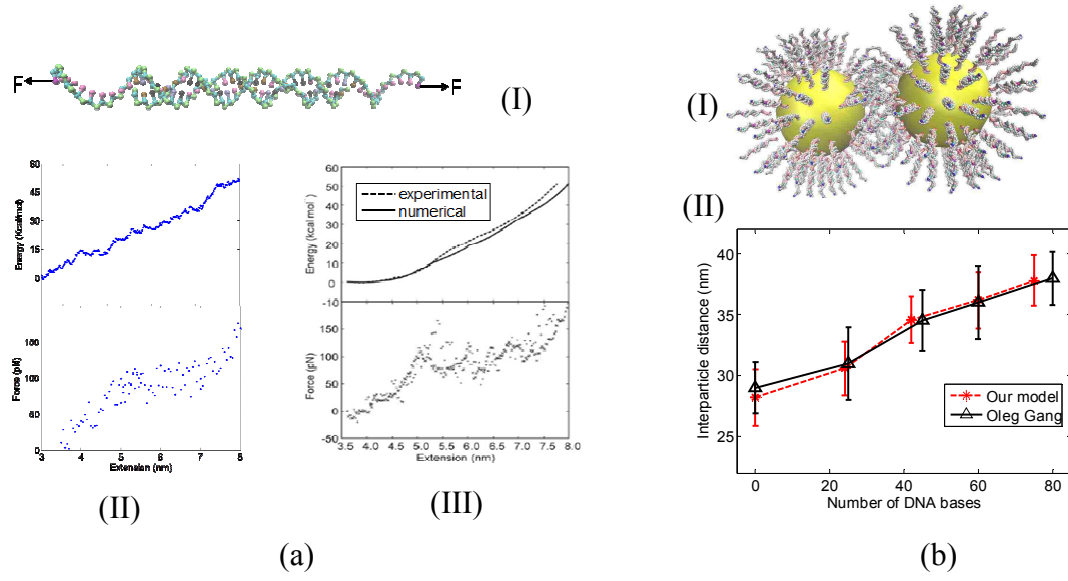


Figure 15. Benchmark cases for the CG model. (a) Mechanical properties of DNA by pulling test. (I), (II) and (III) are the physical settings for the tensile test of DNA strands, the energy/force-extension curves of our model and results reported in Ref.[150], respectively. (b) Internal structure of the dimer assembled by DNA-NP conjugates. (I) is the dimer structure assembled by DNA-NP conjugates, (II) is the comparison of the dependence of inter-particle distance on DNA length (number of DNA bases) of our model and that of Gang *et al.* [151]

With validated DNA-NP conjugate model, the nanoworm structure is assembled and its mechanical properties are studied. Displacement/twisting controlled testing methods are applied to deform the nanoworm. During the stretching process, moving periodic boundary conditions (PBCs) are applied on the X direction. To elongate the nanoworm, the simulation box is extended by 10 nm per nanosecond, as shown in Figure 16 (a). In bending process, a three-point bending test approach is used as depicted in Figure 16 (b): displacements of two end NPs along Y and Z directions are constrained while the middle NP is assigned a displacement of 10 nm per nanosecond along the Y direction. To twist the nanoworm, each end NP is twisted by 30° per nanosecond via opposite directions while the middle NP is set

free, as shown in Figure 16 (c). It should be noted that PBCs are not applicable in the bending and twisting processes, thus the results are slightly affected by the size constraints.

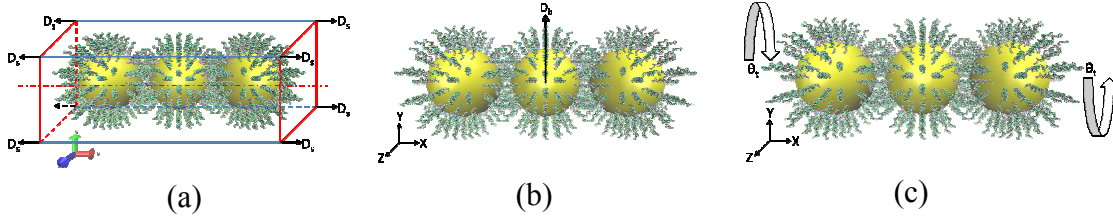


Figure 16. Loading conditions for the nanoworm in processes of (a) stretching, (b) bending and (c) twisting. D_s , D_b and θ_t represent the stretching displacement, bending displacement, and rotating angles, respectively.

To describe the nanoworm's ability to resist deformation and avoid rupture, the stiffness and the strength are imported. The stiffness is defined as the ratio of force applied on the body to the displacement along the same direction of the force during the elastic deformation phase. The strength is defined as the critical energy needed for rupturing the nanoworm. Another parameter, de-hybridization ratio of DNAs (ξ), is also derived to depict the variation of interparticle linkages during the deformations. It is defined as the ratio of the number of instantaneous de-hybridized pairs to the number of original hybridized pairs. The nanoworm is regarded as damaged when ξ is not equal 0 and is treated as ruptured when ξ reaches 100%.

Effects of temperature, DNA coating density and NP size on the mechanical properties of the nanoworm structure are also investigated extensively with this model. Simulations are run by the LAMMPS[65] package with a time step of 1fs at 293 K. The salt concentration is fixed at 100 mM. The dielectric constant for NPs is 11.0[152] while it is 1.0 for biomolecules[34]. The NVE integration is applied to the system with Langevin dynamics representing the Brownian motion of fluid.

3.3. Results & Discussions

In this section, snapshots for stretching, bending and twisting processes of the nanoworm are shown first to illustrate its deformations; then, mechanical properties of the nanoworm are analyzed based on simulation results; next, roles of inorganic and organic molecules in determining the stiffness and strength of the structure are discussed; finally, effects of physical condition and designing parameters on mechanical properties of the nanoworm are described in detail.

3.3.1. Snapshots for stretching/bending/twisting processes

Figure 17 shows a typical stretching process of the nanoworm with an NP diameter of 30 nm, DNA length of 6.8 nm and coating density of 5.35×10^5 strands/ μm^2 at 298 K. The connected DNAs strands between each NP are pulled straight first. Then interparticle linkages are separated gradually through dehybridization. The nanoworm is regarded as ruptured once interparticle linkages no longer exist in the system. The nanoworm stretching is treated as the quasi-static process because no inertia effect is observed.

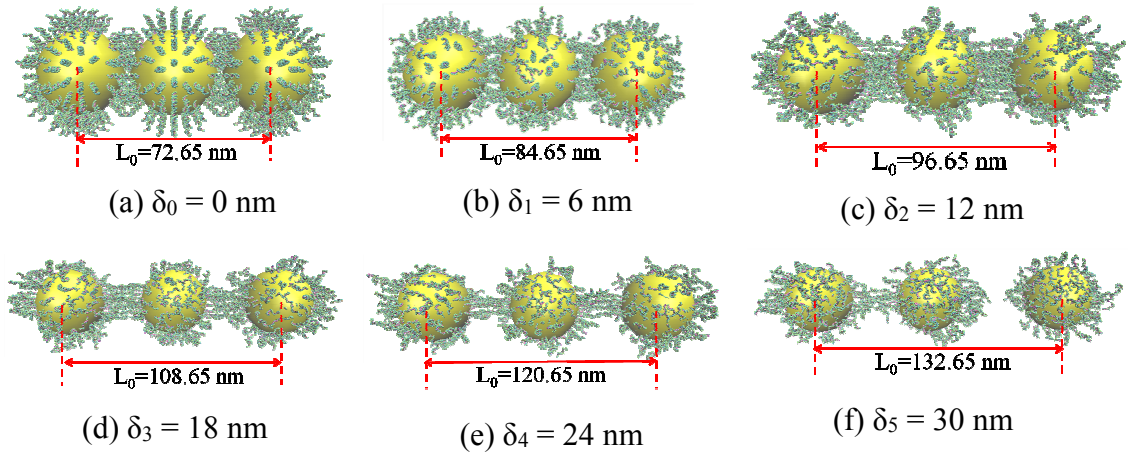


Figure 17. Snapshots for the stretching process of a nanoworm. δ represents the extension which equals $L_n - L_0$ ($n = 0, 1, \dots, 5$).

Figure 18 presents a standard bending process of the nanoworm with the same configuration in stretching process. At early stage, the nanoworm only need to overcome the trivial resistance caused by the original sinuous geometry and ionic interactions; then, the connected strands between each NP are pulled straight, chemical bonds stretching happen during this period; next, dehybridization of linkages starts after the elastic deformation of connected strands reaches maximum state; finally, the nanoworm is ruptured when one NP is isolated from other NPs.

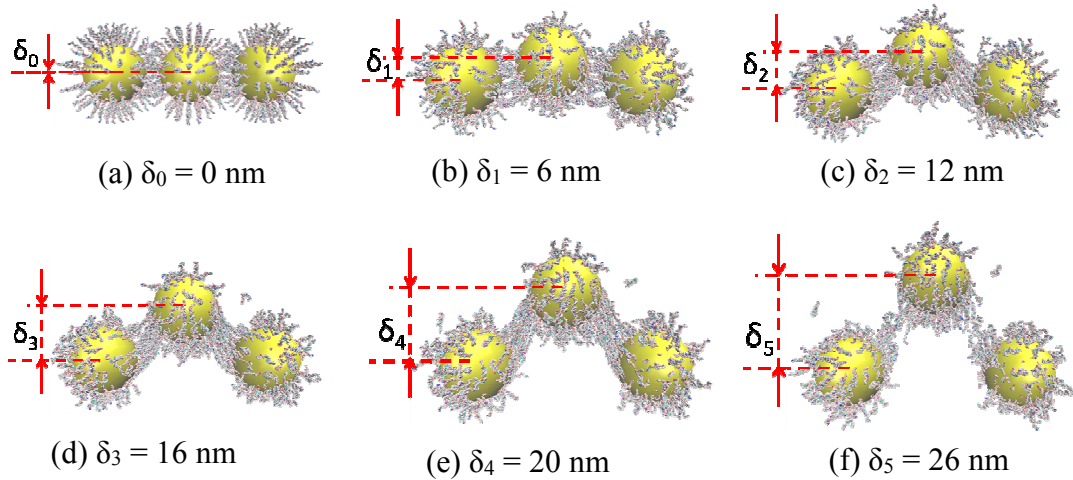


Figure 18. Snapshots for the bending process of a nanoworm. δ represents the deflection.

Figure 19 exhibits the typical twisting process of a nanoworm with the same configuration as that in stretching process. The nanoworm is twisted continuously until it is totally ruptured. To help readers observe how the linkers are broken during this twisting process, strands which still have interparticle linkages are marked as red in Figure 19. Different from stretching and bending processes, the twisting process causes more severe damages to the nanoworm, as shown in Figure 19 (e) and (f). A large quantity of

dehybridizations of DNAs occurs in bridging sections, resulting in disintegration of coating DNAs, which merely happens in stretching and bending processes.

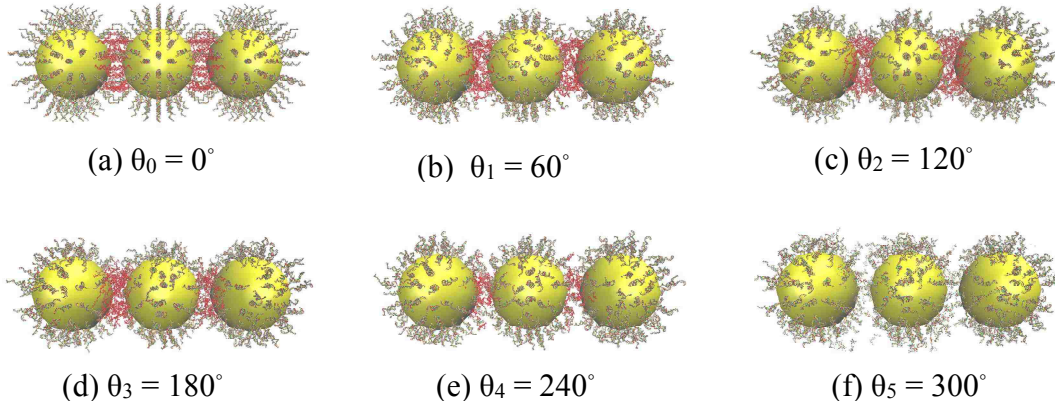


Figure 19. Snapshots for the twisting process of a nanoworm. θ represents the twisting angles. Strands which still have interparticle linkages are marked as red.

3.3.2. Mechanical properties of the nanoworm

Figure 20 shows the energy variation and de-hybridization ratio of nanoworm during deformations. The tested nanoworm has a NP diameter of 30 nm, DNA coating density of 10.7×10^5 strands/ μm^2 , and DNA length of 6.8 nm. During early stages of each process, the nanoworm barely deforms and the energy changes slightly. If continuous displacement/twisting is added, the nanoworm goes through elastic deformation phase and the energy increases rapidly and linearly. At this stage, connected DNA strands are gradually pulled straight without occurrence of dehybridizations; the nanoworm can return to the original structure upon unloading. The strain rate corresponding to the maximum elastic deformation is approximately 75%. However, if external force is continued after the nanoworm has exceeded the maximum elastic deformation, dehybridizations of interparticle linkages occur severely. Deformation of the nanoworm caused by dehybridization of DNA

strands is irreversible, similar to the plastic deformations. Energy crawls up and fluctuates around the peak value when the nanoworm begins to rupture. When the nanoworm is ruptured completely, energy decreases sharply.

The obtained stretching, bending and twisting stiffness of the nanoworm are 42.26, 117.64 and 64.21 $Kcal/(mol \cdot nm^2)$, respectively. Thus, the bending resistance of nanoworm is the largest, followed by twisting and stretching resistances. The critical stretching, bending and twisting energy of the nanoworm are 9407.4, 12269.0 and 13252.4 $Kcal/mol$, respectively. Therefore, the twisting strength of nanoworm is the highest while its stretching strength is the lowest. In another word, the easiest way to deform or rupture a nanoworm is to elongate it. Different from stretching and bending processes, a small energy increment in the twisting process is observed after the nanoworm is ruptured due to severe entanglements of DNA strands.

Dehybridization ratio– extension curves under different deformations are plotted in Figure 20 (b). During each mechanical test, the de-hybridization of DNAs doesn't occur unless at least one connected DNA strand reaches the maximum deformation. The dehybridization happens most violently when the energy reaches the peak value and fluctuates around. The dehybridization ratio reaches 100% when the nanoworm is ruptured completely.

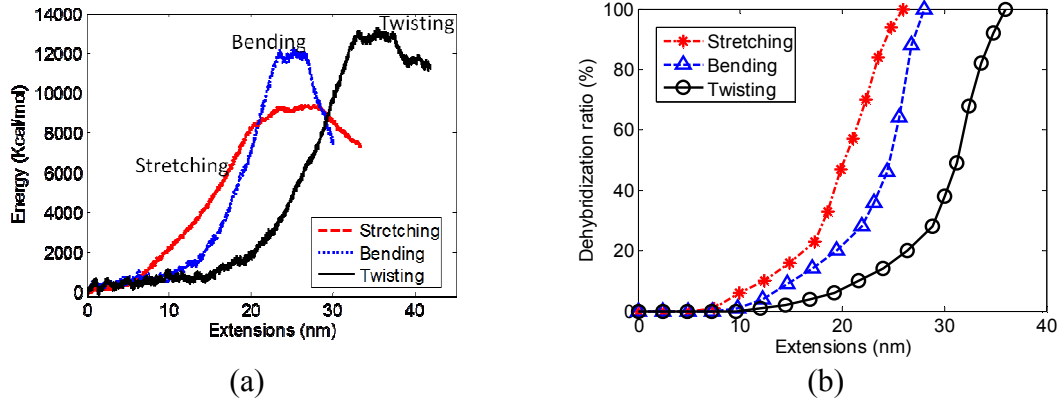


Figure 20. Energy and dehybridization ratio variations during different deformation processes: (a) Energy-extension curves of the nanoworm. (b) Diagram of dehybridization ratio to extension under three mechanical processes.

To study the role of DNA strands in mechanical properties of the nanoworm, energy variations per DNA strand versus deflections of nanoworms with different NP diameters are obtained. The energy-deflection curve for the bending process is analyzed as a representative case, as shown in Figure 21 (a). Both strength and stiffness of the nanoworm with an NP diameter of 10 nm are similar to those with the NP diameter of 30 nm. More importantly, the critical bending energy per strand is about 147.7 Kcal/mol regardless of NP sizes, matching the value of 144.38 Kcal/mol reported by Biswal *et al* [153]. The only difference caused by NP size is the energy wiggles around the peak value for a longer time, which could be explained by more connected strands in larger NPs. Similar results are found in stretching and twisting processes. Thus, it is concluded that the properties of DNA, such as sequences and number of bases, play more essential roles than NP size in determining mechanical properties of the nanoworm. This conclusion is also claimed by Luo *et al.*[154] and Jaeger *et al.*[155].

During the deformation process, total energy (E_{total}) can be divided into two parts: the deformation energy (E_{deform}) to stretch DNA strands, and the de-hybridization energy (E_{dehyb}) to separate originally hybridized pairs. To understand variations of each kind of energies clearly, diagrams of E_{total} , E_{deform} , and E_{dehyb} versus deflections per strand have been plotted in Figure 21 (b). At early moment and elastic deformation stage, E_{total} is mainly used to deform DNA strands. Thus, E_{deform} rises up almost simultaneously with E_{total} . When connected DNA strands reach maximum deformation one after another, dehybridization occurs at interparticle linkages, E_{dehyb} begins to grow while E_{deform} starts decreasing. E_{total} fluctuates around the peak value because decrements of E_{deform} equals increments of E_{dehyb} . When the nanoworm is ruptured, both E_{deform} and E_{dehyb} decline, resulting in a sharp drop in E_{total} .

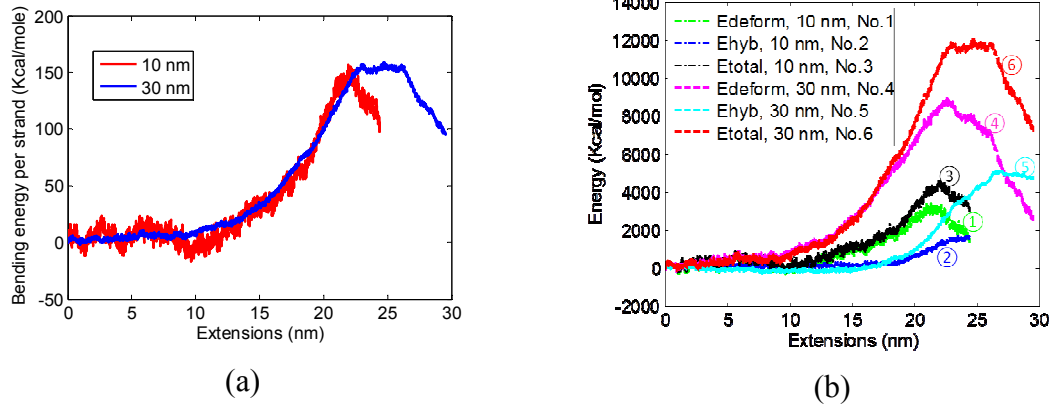


Figure 21. Energy variations per strand during the bending process with different NP sizes. (a) Diagram of bending energy per strand versus extensions. (b) Variations of E_{total} , E_{deform} and E_{dehyb} per strand versus extensions.

To obtain a better design of nanoworms, effects of temperature, DNA coating density and NP size on stretching, bending and twisting properties of the nanoworm are investigated extensively. Considering the length of this paper, only their influences on stretching properties are illustrated.

3.3.3. Effects of temperature

DNA-contained structures are usually refrigerated below 273 K , used in experiments at around 293 K and in human body at 310 K . Thus, properties of nanoworms are studied in the temperature range of $263\text{ K} \sim 310\text{ K}$. To observe effects of DNA melting transitions (melting transition range is $330\sim 360\text{ K}$) on mechanical properties of the nanoworm, the simulation is also carried out at 340 K .

Figure 22 (a) shows energy-extension curves of the nanoworm under different temperatures during the stretching process. From the figure, it can be concluded that at normal temperature range from 263 K to 310 K , the stretching energy changes slowly at small deformation, increases rapidly at the elastic deformation phase, and decreases suddenly after the nanoworm ruptured completely. However, when the temperature is within the transition range of DNAs ($333\sim 353\text{K}$ [156]), energy increases fast even at early small deformations because de-hybridizations of DNA pairs have already occurred at this period. The rupture of nanoworms becomes relatively easy and much less energy is needed for this process. Actually, the nanoworm will be gradually ruptured even without external force when the temperature is within the melting transition range.

Figure 22 (b) and (c) show that mechanical properties of the nanoworm are affected by the temperature nonlinearly. At normal range, the temperature changes both stiffness and strength of the nanoworm slightly. However, once the temperature is beyond the melting

point, its influence on mechanical properties of nanoworm becomes apparent: both the stiffness and strength of the nanoworm at 340 K drop sharply. The stiffness is only 37% of that at 263 K while the strength at is 42% of that at 263 K. Moreover, the nanoworm also becomes very unstable and would decompose automatically given enough exposure time.

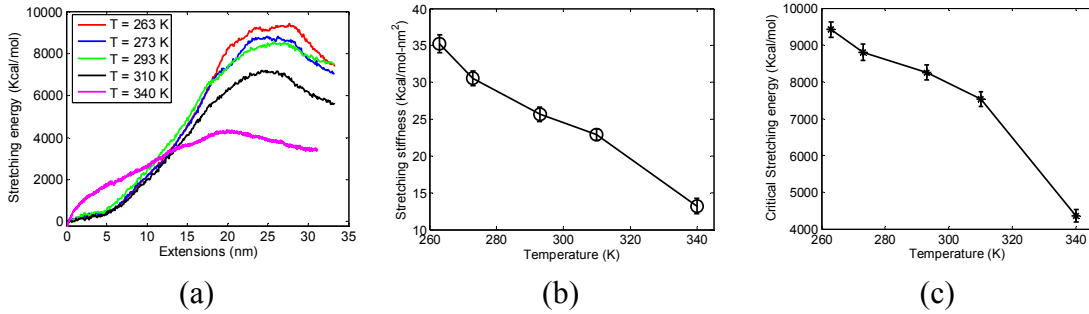


Figure 22. Effects of temperature on stretching property of the nanoworm. (a) Stretching energy versus extension. (b) Effects of temperature on stretching stiffness. (c) Effects of temperature on stretching strength.

3.3.4. Effects of DNA coating density

A set of simulations have been carried out to investigate the quantitative relationship between DNA surface coating densities and mechanical properties of nanoworm. The coating density varies from 1.97×10^5 to 16.05×10^5 strands/ μm^2 , with NP diameter of 30 nm and DNA length of 6.8 nm at 293 K. Effects of DNA coating density on stretching properties of the nanoworm are shown in Figure 23.

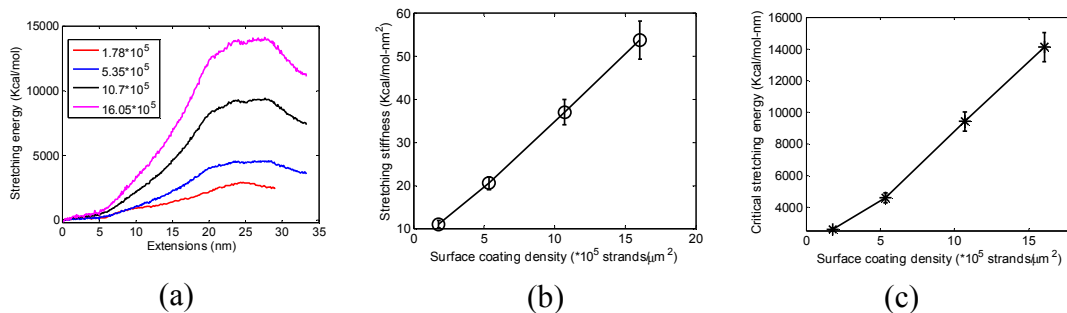


Figure 23. Effects of coating density on stretching property of the nanoworm. (a) Stretching energy versus extension. (b) Effects of coating density on stretching stiffness. (c) Effects of coating density on stretching strength.

Figure 23 (a) shows how diagrams of stretching energy versus extension vary with different surface coating densities. It is found that the coating density doesn't change the configurations of stretching energy – extension curves.

Diagrams of the stretching stiffness and the stretching strength versus surface coating densities are separately shown in Figure 23 (b) & (c). Both stiffness and strength are observed to be linearly proportional to the coating density. With higher surface coating densities, more connected DNA strands are observed between adjacent NPs. This consecutively leads to a more rigid and stronger nanoworm. It should be noted that each connected strand equally enhances the stiffness of nanoworm by $1.58 \text{ Kcal} / (\text{mol} \cdot \text{nm}^2)$ and strengthen the nanoworm by $139.0 \sim 147.1 \text{ Kcal} / \text{mol}$ in the stretching process, similar to results in Figure 21 (a). The total value of stiffness/strength is a multiplication of the stiffness/strength per strand and the number of connected strands. Since there is a linear relationship between the number of connected DNA strands and the coating density, the stiffness/strength of the nanoworm is proportional to the coating density.

3.3.5. Effects of NP sizes

To study effects of NP size on mechanical properties of the nanoworm, a set of simulations are carried out with different NP diameters varying from 10 nm to 110 nm. Here, the coating density is fixed while numbers of strands on NPs vary with diameters.

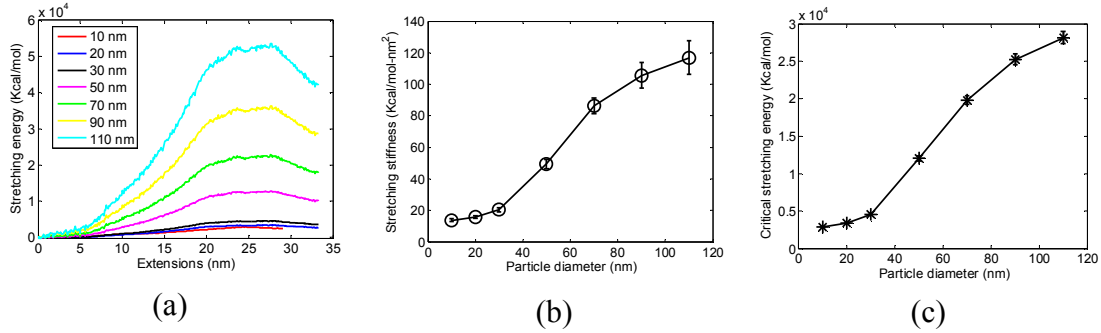


Figure 24. Effects of NP diameters on stretching processes of the nanoworm. (a) Stretching energy versus deflections. (b) Effects of NP diameter on stretching stiffness. (c) Effects of NP diameter on stretching strength.

Figure 24 (a) depicts the stretching energy versus extension with different NP sizes. It is found that all energy profiles are independent of NP sizes. Figure 24 (b) and (c) show effects of NP diameter on stretching stiffness and strength of the nanoworm, respectively. Both stiffness and strength increase nonlinearly with an increasing diameter. When NPs diameters are smaller than 30 nm, the stiffness and strength of nanoworm increase slowly as NPs become bigger. However, when the NP diameter is within the range of 30 ~ 70 nm, the stiffness and strength rise up much more rapidly. After the NP diameter exceeds 70 nm, the growing ratio of the stiffness/strength becomes relatively small again.

It has been demonstrated that the number of connected DNA strands directly determines the mechanical properties of nanoworms in Figure 21 (a). Thus, the influence of NP diameters on mechanical properties of nanoworm can be resolved by effects of NP

diameter on number of connected DNA strands. The NP size determines the number of connected strands between adjacent NPs are affected by NP size from three mechanisms: firstly, a larger NP has more surface area which enables more DNA strands coated onto it; secondly, a bigger NP has a larger hybridization area within which interparticle linkage is possible[107]; thirdly, a larger diameter of NPs has a smaller curvature that leads to a smaller orientation angle of coated DNA strands[157]. The first two mechanisms enhance the possibilities to form connections between adjacent NPs but the third one has reverse effects. Besides, NP itself has little effects on mechanical properties of the nanoworm since the studied NPs are relatively small that they have no contact with each other due to the densely packed DNA shell. In the future, the weight of each mechanism on determining mechanical properties of nanoworm will be investigated, with the particle size ranging from nanometers to micrometers. This will provide a more profound understanding about effects of particle size on mechanical properties of the nanoworm.

3.4. Conclusions

A CG MD model has been developed to study mechanical properties of nanoworms under different physical conditions. The model was validated by the fact that both mechanical and structural properties of our model agree well with those reported in literature.

Simulation results show that the deformations of nanoworm are mainly caused by two parts: elastic deformation of DNA strands and dehybridization of interparticle linkages. The deformation of nanoworm cause by the former one can be regarded as reversible elastic deformation while that by the latter one is similar to irreversible plastic deformation. In addition, the nanoworm is most prone to be deformed and be ruptured by a stretching force.

It is also found that DNA is the main determinant for mechanical properties of the nanoworm. Contributions of each connected DNA strand to the stiffness and strength of the nanoworm are almost the same.

At low and normal temperature range, the stiffness and the strength of the nanoworm decrease slightly with a rising temperature. However, when the temperature goes into the melting transition range, both stiffness and strength of the nanoworm are reduced extensively because dehybridizations can occur without external force. The nanoworm can even decompose automatically at high temperature. Meanwhile, the coating density affects mechanical properties of nanoworm by determining the number of connected DNA strands between adjacent particles. Since a linear relationship exists between the number of connected DNA strands and the coating density, the stiffness and strength increase almost linearly along with the coating density. Moreover, a larger NP size leads to a stiffer and stronger nanoworm because more connections are formed between adjacent NPs when particles are larger. It is also observed that the relationship between NP size and stiffness/strength of nanoworm is nonlinear.

In conclusion, all physical and structural parameters indirectly influence the stiffness and strength of nanoworms by directly changing properties and quantities of interparticle linkages. The results of this paper can serve as guidance for better designs of nanoworms which have versatile potential applications. As consecutive future work, more complex 2D and 3D nano-structures will be assembled by DNA-NP conjugates and their mechanical properties and potential applications will be studied.

3.5. Acknowledgements

The authors acknowledge the supports for this work from National Science Foundation Grant Nos. CBET-1067502 and CBET-1113040 for Y.L..

4. Mechanical response and potential application of nanosheet by DNA-NP conjugates

Two dimensional nanosheet of DNA-nanoparticle conjugates have become a promising platform for developments of chemical sensor, molecular circuit, and mechanical analysis tools. Whatever it is used for, the mechanical properties affect its efficiency and efficacy in large extent. Thus, a coarse-grained molecular dynamics simulation model has been developed to study its mechanical responses under different loadings. Stress-strain curves of the lattice are obtained from biaxial stretching and shearing tests and analyzed. Effects of hairpin loop structures on mechanical properties of the nanosheet have been exclusively studied. Results found they determine the mechanical properties of nanosheet significantly. Physical conditions such as the temperature and salt concentration on mechanical response of the nanosheet are also discussed. Numerical models for critical forces to elastically deform and rupture the nanosheet have been built up, with its accuracy validated by simulation results. Force-strain curves also indicate the nanosheet behave like a foil sheet. The area expansion modulus is found to be $3.44 \times 10^2 \mu N / m$ and the shear modulus is $6.07 \times 10^4 Pa$. Results of this article can serve as guidance for applying nanosheet as a flexible strain sensor.

4.1. Introduction

DNA- nanoparticle (NP) conjugates[74] have been treated as potential building blocks[75, 76] for complex, self-assembling materials[77-84] for their versatile chemical[89, 91-97] and physical[76, 84, 88-90, 100] properties from introduced by Mirkin *et al.* in

1996[84]. Structures assembled by DNA-AuNP conjugates can be classified into three main categories: one-dimensional[107, 158-163] (1D), two-dimensional[83, 103, 164-166] (2D) and three-dimensional[82, 83, 85, 167-173] (3D) assembly. A 1D nanoworm structure has been created by self-assemblies of DNA-NP conjugates and its mechanical properties have been studied extensively by coarse-grained molecular dynamics. In this article, a 2D nanosheet is assembled by DNA and NP conjugates as a consecutive work.

Bottom-up fabrications of 2D sheet by DNA and AuNP conjugates have been developed by many researchers. Established methods to form 2D lattice of DNA-NP conjugates have been successfully developed on both solid and liquid surfaces through continuous efforts. Currently main techniques for self-assembling ordered monolayer arrays of DNA-mediated nanoparticles on solid surfaces include three general categories[174]: (1) distributing colloidal suspensions on the solid substrate by drop-casting[175, 176] or spin-coating[177] and then dry the solvent; (2) depositing the colloidal suspension onto the solid substrate by field-enhanced[178, 179] or molecular interaction-induced[180-184] methods; (3) spreading the colloidal suspension of hydrophobic particles on water surfaces, then evaporate the solvent, and subsequently transferring NP arrays to solid substrates by Langmuir-Schaefer technique[185, 186]. Currently most 2D arrays of DNA capped nanoparticles are formed on solid substrate surfaces[174, 184, 187-189], but there is an inherent problem in all methods of self-assembling on solid substrate: few solid surface are uniform on the nanoscale[174]. Thus, some researchers also formed the 2D sheet on liquid surfaces[103, 190, 191].

The nanosheet assembled by DNA-AuNP conjugates are commonly used as chemical sensors to inspect environmental conditions[174], biosensors to detect cancer cell[187],

genetic information collection platform[93, 192, 193], as well as molecular electronics devices[189, 191, 194-196]. The importance of mechanical properties on its performances has been demonstrated by Nienke Geertz and Erika Eiser[197] in 2010. Oleg Gang *et al.*[103] and Dan Luo *et al.*[154] studied mechanical properties of the 2D nanosheet and found them behave like a macroscopic paper or alumina foil: their force-displacement relationships are in agreement with the scaling law of elastic sheet[198]. However, a thorough understanding about the relationship between stress and strain of the 2D nanosheet has yet to be fulfilled.

To study the mechanical properties of 2D nanosheet assembled by DNA-NP conjugates, a coarse-grained molecular dynamics model for the 2D nanosheet has been developed with the same force fields in the last paper. Stress-strain curves of the 2D sheet under shearing and stretching will be analyzed with different physical conditions. Effects of connecting DNA structures on mechanical properties of the 2D nanosheet will also be studied. In addition, the reproducibility and reliability of mechanical properties of this 2D array are evaluated. Based on simulation results, a numerical model will be proposed for the elasticity of the 2D array. In future, the numerical model will be evaluated by our experimental results.

4.2. Methods

Potentials for the system are the same with those to study the mechanical properties of nanoworm. Different from the fact that only one type of DNA structure are used for assembling nanoworm, two types of DNA strands are utilized in the nanosheet system: the single stranded DNA as coating molecule and the hairpin loop serving as connecting DNAs between NPs. Structure and sequence designs of these two DNA types are shown in Figure 25 (a) & (d). The assembling process of nanosheet can be categorized as two stages:

fabricating conjugates by coating ssDNA onto NPs and assembling the nanosheet by connecting conjugates with hairpin loops. Figure 25 (e) shows a full model of nanosheet and (f) represent a simplified one with all coating DNA hidden for clarifying connections between each NP. The diameter of NPs used in the system is 10 nm. DNA surface coating density is fixed at 5.35×10^5 strands/ μm^2 . All physical conditions are set the same as that of the experimental work of Dan Luo *et al.*[154], in order to be comparable with their results.

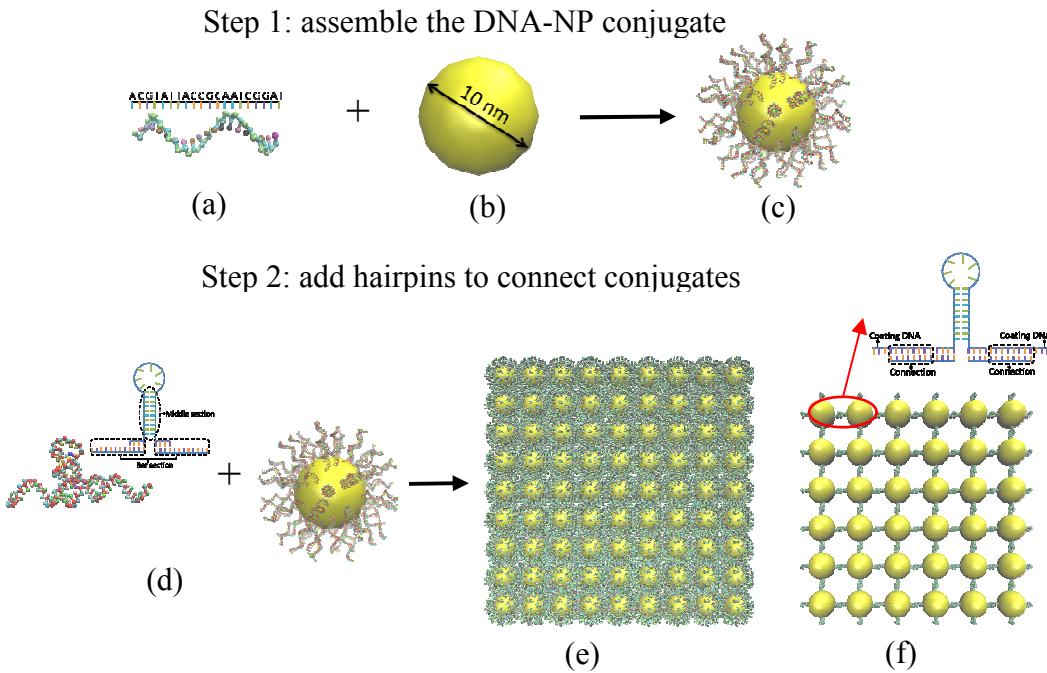


Figure 25. Constructing 2D nanosheet with DNA-NP conjugates. (a) Coating DNA, (b) NP, (c) conjugate, (d) hairpin loop, (e) full nanosheet model, (f) simplified nanosheet model

Two benchmark cases were carried out to validate the CG MD model. The first one was to validate mechanical behaviors of DNA hairpin loops. A DNA hairpin loop was stretched and its energy/force-extension curve was obtained, as shown in Figure 26. Results are found to agree well with experimental data[199], indicating that the our model has successfully captured mechanical characteristics of the DNA hairpin loop.

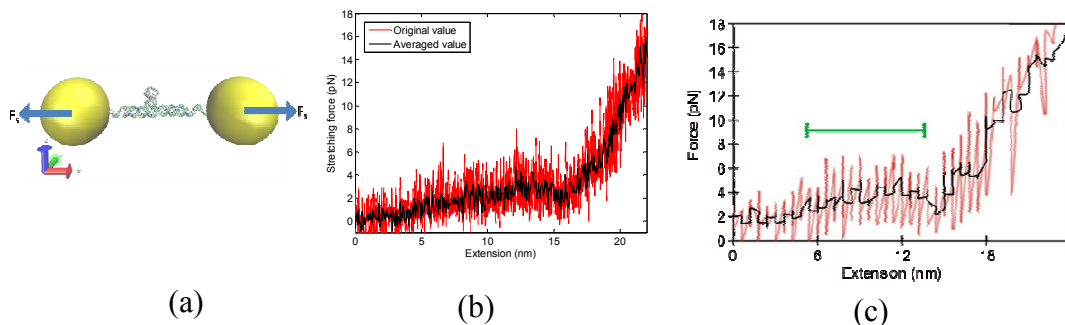


Figure 26. Benchmark case for the mechanical behavior of DNA hairpin loop. (a) Initial setup for the hairpin loop stretching. (b) Force/extension curve of our model. (c) Experimental data for force/extension curve[199, 200]

The second benchmark case is to compare the hardness of nanosheet obtained from our model with literature data. A nanosheet with DNA-AuNP conjugates arrays was assembled with the same physical parameters as those in the work of Luo *et al.*[154]. A displacement controlled indentation method is applied to the system as depicted in Figure 27 (a). All degrees of freedom of peripheral NPs were fixed to avoid the rigid motion and rotation of the nanosheet. A displacement of 1 nm per ns was assigned to the middle NP along the negative Z direction. The force-displacement curve (Figure 27 (b)) was obtained from our system and compared with that from Luo *et al.*[154] in Figure 27 (c). A good agreement was found between our results and the work of Luo *et al.*, indicating that our model has captured key characteristics of the 2D nanosheet.

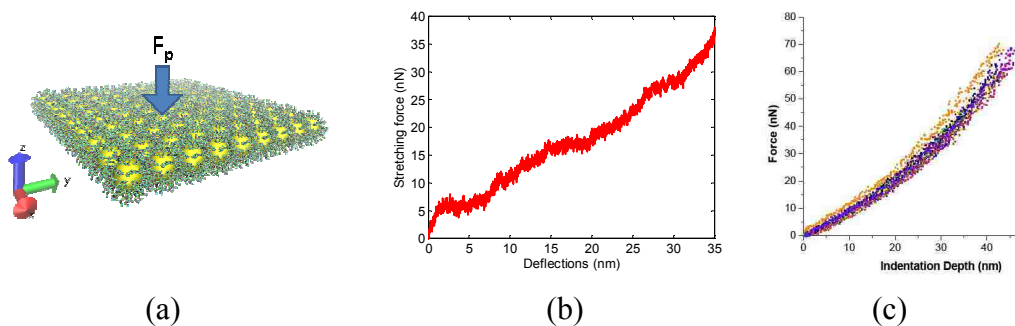


Figure 27. Indentation testing of the 2D nanosheet as a benchmark case. (a) Physical settings for the indentation. (b) Force-displacement curve of our model. (c) Force-displacement curve obtained by Luo *et al.*[154]

After establishing the nanosheet model, uni-axial stretching, area expansion and shearing tests of the 2D nanosheet were carried out with a displacement-controlled method, as shown in Figure 28. Instead of directly adding displacements to particles, we control the motion of all molecules by deforming the simulation box. The advantage of deforming the simulation box is no energy concentration, which might be caused by non-uniform control of particles, will appear in the system. To mimic a quasi-static deformation process, the stretching or shearing speed is so slow that kinetic energy of the system can be controlled to approximately zero. Periodic boundary conditions (PBCs) are applied in both X and Y directions to exclude the size effects on mechanical properties. Effects of structural parameters like sequences and numbers of bases in middle or bar sections of hairpin loops on mechanical properties of 2D nanosheet assembled by DNA-NP conjugates are extensively studied. Simulations are run by the LAMMPS[65] package with a time step of 1fs at 293 K. The salt concentration is fixed at 100 mM. The dielectric constant for NPs is 11.0[152] while it is 1.0 for biomolecules[34]. The NVE integration is applied to the system with Langevin dynamics representing the Brownian motion of fluid.

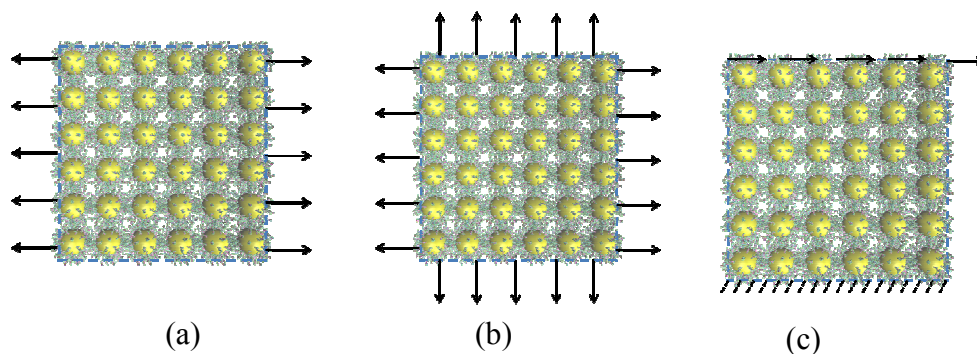


Figure 28. Displacement controlled (a) uni-axial stretching, (b) area expansion and (c) shearing tests of the 2D nanosheet.

4.3. Results and Discussions

4.3.1. Snapshots for stretching /shearing tests

Uniaxial-stretching, area expansion and shearing tests have been carried out to extract mechanical characteristics of the nanosheet. Snapshots for these different tests have been captured for a better understanding of deformation of the nanosheet. Results find that the uniaxial-stretching and area expansion share a lot of similarities in deformation, energy and force variations. Considering the compactness of this article, only the uni-axial stretching and shearing tests are analyzed in detail. Snapshots and energy/force profiles for the area expansion process can be found in the Supporting Information.

Figure 29 shows the deformation of nanosheet under stretching process. During the stretching test, the nanosheet was pulled from X direction with free motion in Y direction. the deformation of nanosheet consists of four different stages: firstly, the connection between NPs which are double stranded DNA were pulled straight; secondly, hairpin loop unzipped; thirdly, the unzipped hairpin loop, which turned to be single strand, was pulled straight (this phenomenon happens very fast); lastly, connections between NPs, which are

bridged by hybridizations between coating DNAs and the bar section of hairpin loop, begin to be separated, the rupturing of nanosheet started.

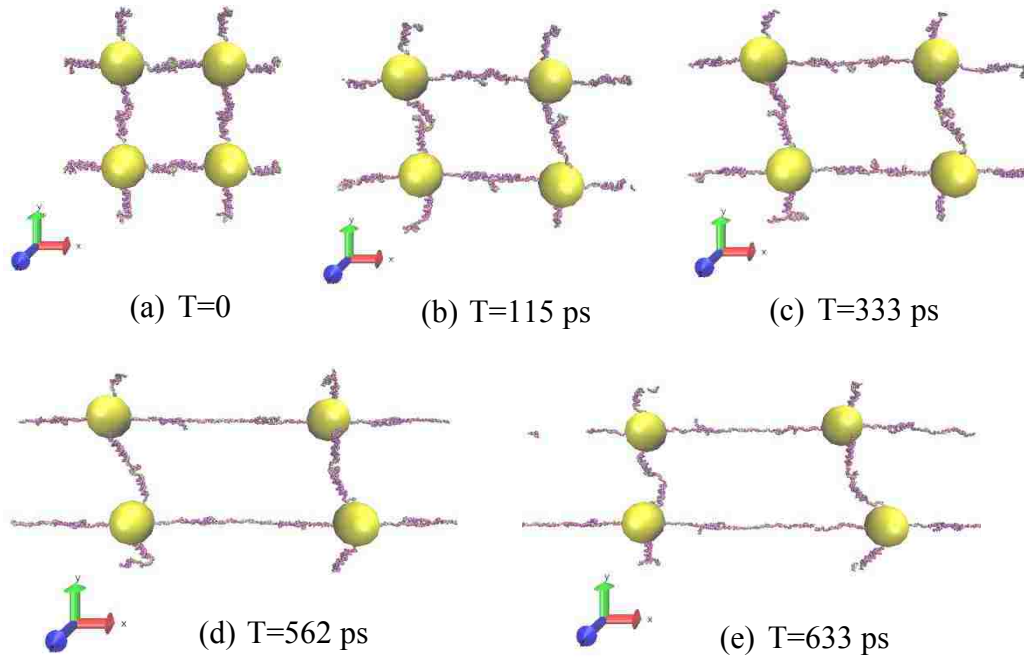


Figure 29. Snapshots for area expansion process. For clarity, coating DNAs were hidden

As shown in Figure 30, the nanosheet went through four similar stages with that under uni-axial stretching.

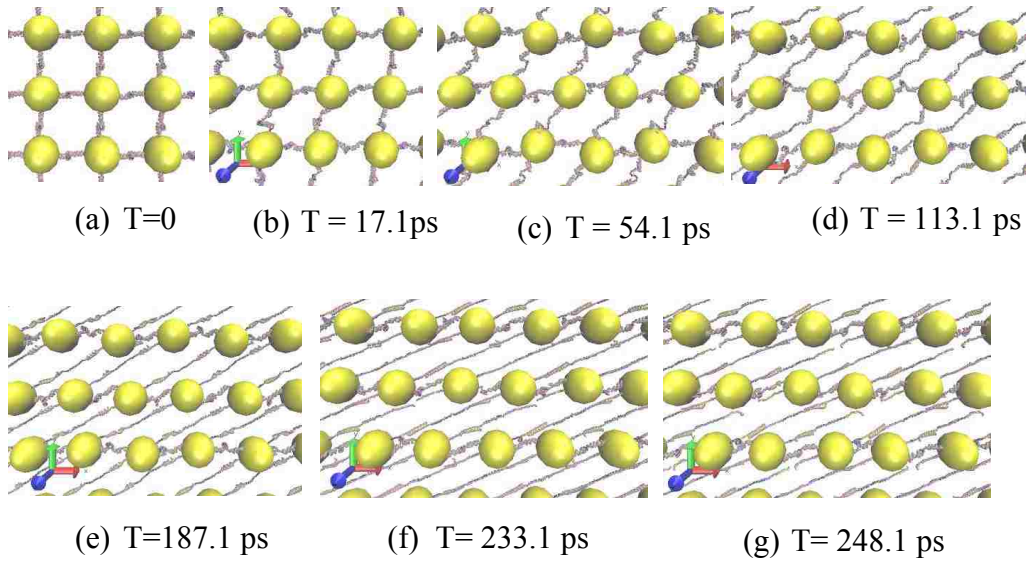


Figure 30. Snapshots for the shearing process of the nanosheet. For clarity, coating DNA were hidden

4.3.2. Energy/Force-Extension Curves

Time histories of energy for the whole system during the deformations are shown in Figure 31 (a). In all processes, an initial energy is seen to deform the box. Then, a small energy jump is observed to unzip the hairpin loop from middle sections. Thirdly, a peak value of energy is detected for breaking the connections between NPs. More energy is needed to rupture the nanosheet by shearing than by stretching. It could be explained by the fact that more connections needed to be broken when shearing. In addition, the energy needed for the area expansion is two times of energy for uni-axial stretching, corresponding to the nature of the area expansion is a multiplication of two uni-axial stretching.

Force-extension curve and force-shear angle of the nanosheet for stretching is also shown in Figure 31 (b) & (c). For reliability, these profiles are obtained by averaging 6 simulations data. It can be known from the figure that a larger force is needed to unzip the

hairpin loop from the middle section. Once the hairpin is unzipped, a small drop is observed in the curve because the unzipped hairpin loop is stretched. After the hairpin loop reached maximum stretching, a much larger force is called for breaking the connections between NPs. During this step, the bar section of the hairpin loops are broken and the nanosheet is ruptured consequently.

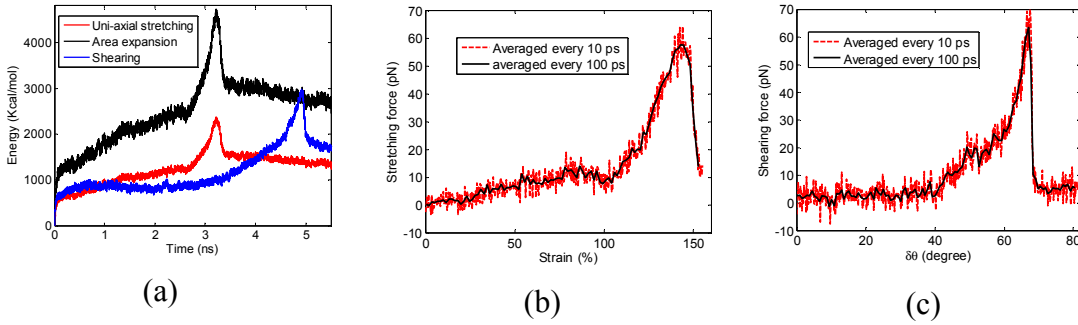


Figure 31. (a) Time history of Energy during the stretching and shearing processes. (b) Force-extension curve during the stretching process. (c) Force- shear degree curve during the shearing process

4.3.3. Effects of DNA Hairpin Loop Structures

To investigate effects of DNA hairpin loop structures on mechanical properties of the 2D nanosheet, three different hairpin loops have been designed and used to assemble the nanosheet. Connections formed by coating DNAs and these different hairpin loop structures are depicted in Figure 32 (a) ~ (c), assembled nanosheets are shown in (d)~ (f).

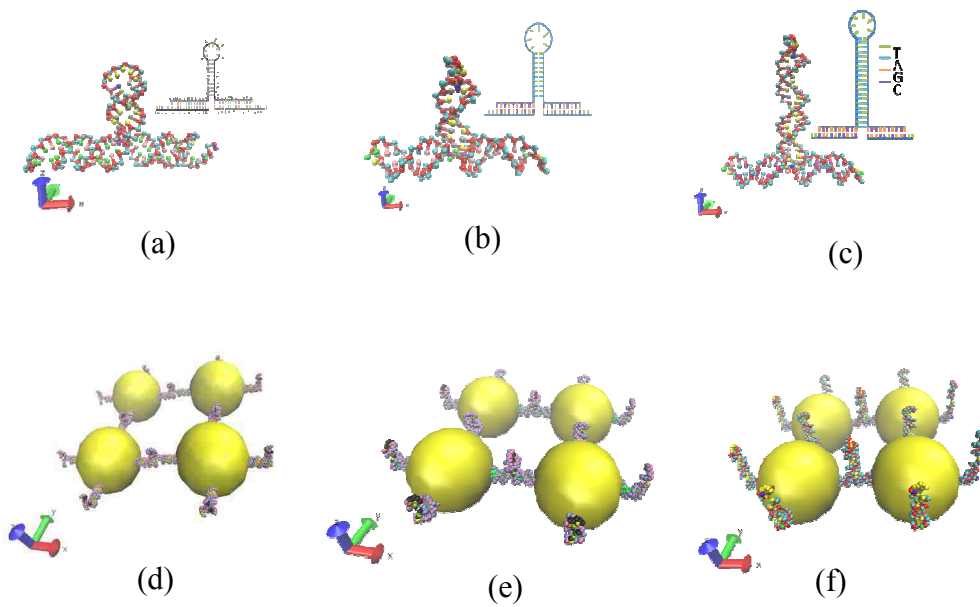


Figure 32. Different types of hairpin loop structures and the correspondingly assembled nanosheets. To show how these hairpin loops serve as connections between NPs, the coating DNAs of nanosheets are hidden.

One key point in our model is the hairpin loop have to be unzipped from the middle section first. A set of simulations have been run to test what kind of hairpin loop structures satisfy our requirement, detailed in the Supporting Information. It is found that the hairpin loop should have more C-G pairs in bar sections to make sure the loop will be unzipped before the bar sections totally dehybridized from coating DNAs. If the number of C-G pairs in the bar section is less than half number of the pairs in middle section, the hairpin loop is not appropriate to be used as connections because the hairpin loop will break from the bar section first no matter how slowly it is pulled. To check the availability of these hairpin loop structures as connections, the stretching test was carried out for each structure similar to the first benchmark case.

After three types of nanosheet were assembled with different hairpin loops as connections, their stretching and shearing behaviors were tested. As shown in Figure 33, mechanical behaviors of the nanosheet are mainly determined by the structure of hairpin loops, especially the number of C-G pairs in the middle and bar sections. A larger force is needed to deform the nanosheet if more C-G pairs are contained in the middle section. Similarly, if more C-G pairs are contained in the bar section, bigger forces are required to damage the nanosheet.

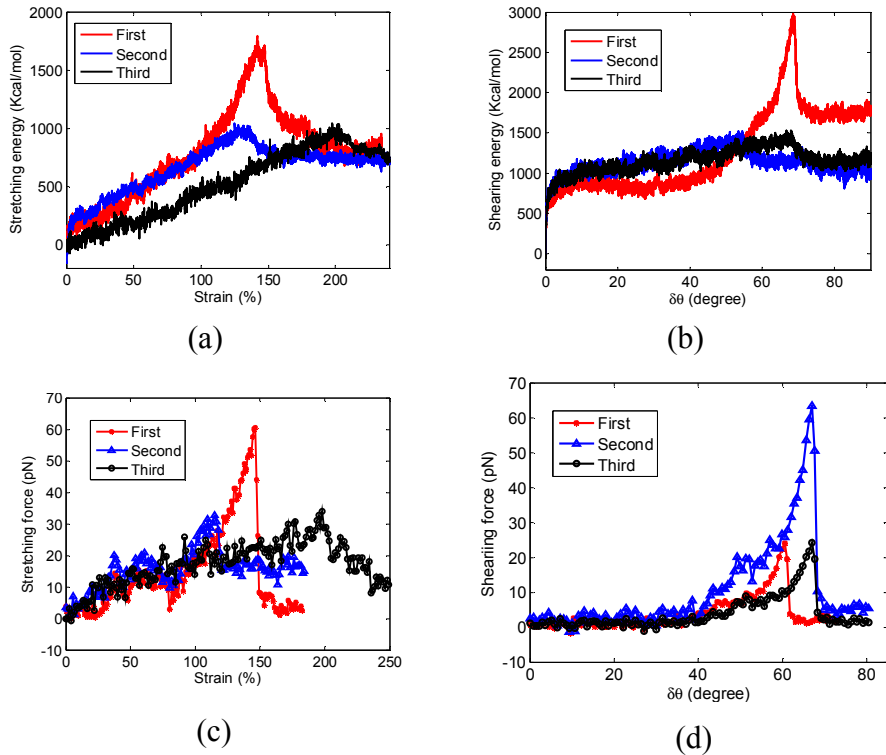


Figure 33. Effects of hairpin loop structures on mechanical properties of nanosheet. (a) Energy-extension curve for stretching process. (b) Energy-strain curves for stretching process. (c) Force-extension curve of the nanosheet for stretching process. (d) Force-shearing degree curve of the nanosheet for shearing process.

From the force-extension curves of nanosheets with different hairpin loop structures as connections, it is easily seen that the hairpin loop structure affect the mechanical properties of nanosheet from two aspects. Firstly, the number of C-G pairs in the bar section determines how much force is needed to rupture the nanosheet. Secondly, the number of hybridization pairs in the middle section of the hairpin loops is more related to the extensions of nanosheet. It could be explained by the deformation process of the nanosheet. Four deformation stages exist in the whole process: firstly, the connection as double strands extended slightly, the deformation of nanosheet should only overcome resistance brought by the salt concentration and nature relaxed configuration of the connections. It should be noted that the extension is very small and the energy variation is slight because no chemical bond stretching occurs at this stage. Secondly, connections between nanoparticles are straightened, chemical bonds in DNAs are stretched, leading to a quasi-linear force-strain relation. Thirdly, hairpin loops in connections unzipped slowly, pre-quenched fluorescent signals are released out and captured by SEM and transformed to strain information. After all pairs in the hairpin loop section are separated, the hairpin loop becomes a straight single strand whose ends are still connected to the coating DNAs. As the nanosheet is continuously pulled, dehybridization process happened in the bridge section. Compared to unzipping hairpin loops, dehybridizing the bridges calls for much larger forces, that's why we observed a big increment in the force-strain curves. Actually this offers convenience for experimental operations when using the nanosheet as the strain sensor due to the extinguished force difference between unzipping hairpin loops and dehybridizing bridges.

4.3.4. Numerical Model for Threshold Force Values

Two force peaks are observed from the force-strain curves of CGMD nanosheet: the first one is for completely unzipping hairpin loops (F_{un}), the second is for rupturing the nanosheet (F_{ru}). When the external force exceeds F_{un} , the originally quenched fluorescence in hairpin loops are released out and used as signals to represent strains. Once the load of nanosheet exceeds F_{un} , the hairpin loops are completely unzipped and turned out to be a single strand. If the external force is continuously loaded, the single strand which is transformed from hairpin loop will be pulled straight. This process happened very fast and a drop of force is observed. Once the deformation of single strand reaches the maximum state, connections between the hairpin loop and coating DNAs begin to be split. This should be prevented because it will cause the rupture of nanosheet. Thus, the maximum force should be no bigger than F_{un} . Considering the fact that F_{ru} is usually four to five times larger than F_{un} , we could conclude that there is a safe force region which allows the releasing process of fluorescence without rupturing the nanosheet, as shown in Figure 34.

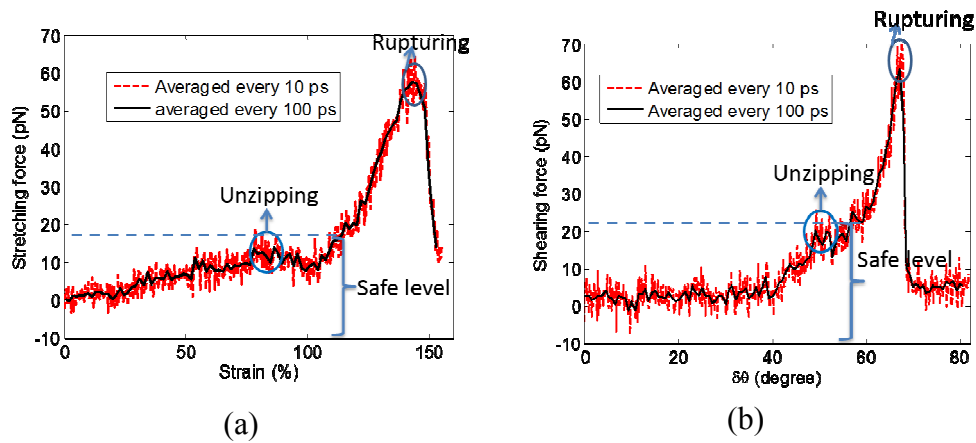


Figure 34. Safe level of force range in (a) stretching test and (b) shearing test

It is found that both F_{un} and F_{ru} for a nanosheet are determined by the structures of hairpin loops. F_{un} is determined by the sequences and number of pairs in the hairpin loop structure while F_{ru} can be calculated from the sequences and number of pairs in the bar section of hairpin loops. As has been stated by other researchers, the force for separating a C-G pair is 4.18 pN while that for separating an A-T pair is 1.38 pN, relationship between F_{un} and structures of nanosheet can be expressed as

$$F_{un} = \left(\frac{l}{l_0}\right)^2 \cdot (4.18a_m + 1.38b_m) \cdot \eta_T \cdot \eta_C \quad (\text{Eqn. 24})$$

Where l denotes the length of the nanosheet, l_0 , a_{loop} , b_{loop} , η_T and η_C represent the initial interparticle distance, number of C-G pairs and number of A-T pairs in the loop section of hairpin loop structure, temperature scaling factor, and salt concentration scaling factor respectively.

Similarly, relationship between F_{ru} and structures of nanosheet can be modeled as

$$F_{ru} = \left(\frac{l}{l_0}\right)^2 \cdot (4.18a_b + 1.38b_b) \cdot \eta_T \cdot \eta_C + F_{un} \quad (\text{Eqn. 25})$$

where a_b and b_b indicate the number of C-G pairs and number of A-T pairs in the bar section of hairpin structure.

The determination of temperature scaling factor and salt concentration scaling factor are discussed below.

4.3.5. Temperature/Concentration Scaling Factors

In order to get the temperature scaling factor, a set of simulations have been run to obtain mechanical characteristics of nanosheet under different temperatures. As shown in Figure 35(a) and (b), temperature has little effects on both stretching and shearing processes

of the nanosheet during the normal range. Only when the temperature is within the melting transition range, the nanosheet becomes unstable due to the occurrence of hybridizations of DNAs. The structure is easier to be ruptured, resulting a weaker strength and unseen transition of being ruptured. Since the nanosheet is usually restored and applied under melting point, we only consider the temperature at 273, 293, 303 and 313 K. To get a normalized temperature scaling factor, all mechanical data obtained from different temperature points are divided by those obtained data at 293 K. Thus, η_T at different temperatures are tabulated in Table 4. Each data was averaged by four simulations whose differences only lay on their slightly changed initial coordinates of atoms.

Table 4. Temperature scaling factors

Temperature (K)	273	293	313
η_T	1.067	1	0.933

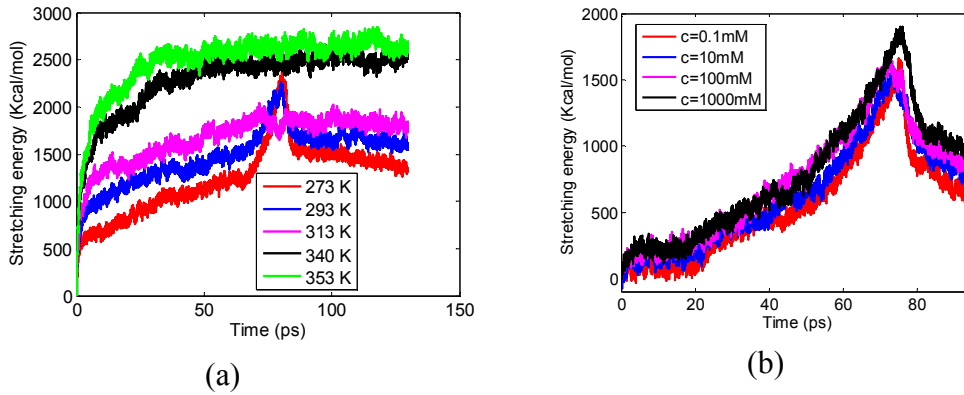


Figure 35. Effects of temperature on Mechanical properties of nanosheet. (a) Effects of temperature on free energies in stretching process. (b) Effects of salt concentration on free energies in shearing process.

The concentration scaling factor can also be calculated following the similar approach of obtaining the temperature scaling factor. To understand how ionic concentrations affect the mechanical behavior of the nanosheet, a set of simulations were carried out under different salt concentrations, ranging from 0.1 mM to 1000 mM. As shown in Figure 35 (b), the effects of salt concentration on nanosheet are not very significant, almost linear. Following the same normalizing method with temperature section, the concentration scaling factors are obtained and tabulated in Table 5.

Table 5. Salt concentration scaling factor

Salt concentration (mM)	0.1	10	100	1000
η_c	0.847	0.924	1.000	1.002

4.3.6. Evaluation of numerical model

To evaluate the accuracy of our numerical model, a series of simulations with different initial configurations under different conditions have been carried out. F_{un} and F_{ru} of each system have been analyzed from the simulation results and compared with numerical data.

Table 6 has listed a portion of test work with different initial setup, their simulation results and numerical results are also included. For reliability of results, each data is the average value of results obtained by four different simulations. These four simulations have the same initial structural parameters and environmental factors, their only difference lies on the slightly changed coordinates of some atoms without changing the total energy of the system after minimization. The calculated F_{un} from these simulations have been compared with numerical results. It is found that the difference between the simulation results and numerical results are within 5%. Thus, our numerical model has high accuracy and can be

used to predict mechanical characteristics of the nanosheet. In future, the numerical model will also be evaluated by experimental results, subsequently. It should be noted that simulations included in Table 6 is mainly used to clarify the initial configuration parameters, more clarity cases are shown in the Supporting Information. Based on test samples, a good agreement has been illustrated between the simulation results and numerical results.

Table 6. Comparison between simulation results and numerical results under different situations

#	Initial configuration						C (mM)	T (K)	Simulation (pN)		Numerical (pN)	
	n_b	n_b^{CG}	n_b	n_b^{CG}	l (nm)	l_0 (nm)			F_{in}	F_m	F_{in}	F_m
1	30	10	20	10	145.6	23.6	100	293	890.2	2002.1	889.6	2000.0
2	30	20	20	10	145.6	23.6	100	293	890.0	2447.5	889.6	2448.0
3	20	10	20	10	145.2	23.6	100	293	889.9	1780.0	889.6	1779.2
4	20	10	20	20	146.0	23.7	100	293	1336.8	2225.5	1337.6	2227.2
5	20	10	10	10	53.6	13.4	100	293	668.0	1560.1	668.8	1558.4
6	20	20	10	10	53.6	13.4	100	293	668.5	2006.9	668.8	2006.4
7	20	10	10	10	53.7	13.4	10	293	616.2	1211.7	618.0	1214.1
8	20	10	10	10	53.6	13.4	100	273	715.0	1667.1	713.6	1662.8
9	20	20	30	20	121.6	30.4	100	273	1664.5	3093.1	1662.8	3090.0
10	20	20	30	20	121.6	30.4	1000	293	1560.6	2900.9	1561.5	2901.7

- ✧ n_b —number of bases in hairpin loop section
- ✧ n_b^{CG} —number of C-G bases in hairpin loop section
- ✧ n_b —number of bases in the bar section
- ✧ n_b^{CG} —number of C-G bases in the bar section
- ✧ l —edge length of the nanosheet
- ✧ C —salt concentration
- ✧ T —temperature

4.3.7. Material properties of nanosheet

After aware of the safe force range, the area expansion modulus of the nanosheet will be discovered. To ensure the synchronization of fluorescence signals and strains, the nanosheet is pre-stretched until the connection between coating DNA and hairpin loop section are stretched to the ultimate state without hairpin loop unzipping. Under such initial settings, the fluorescence signals can be directly used to indicate the strain of nanosheet. Then, the nanosheet is bilaterally expanded. The expansion rate is small enough that the kinetic energy of the system can be ignored, so the expansion process can be regarded as quasi-static process. The force-strain curve of the nanosheet during this period is shown in Figure 36 (b). Referring to the work of Lenormand et al.[201], the area expansion modulus is described by the linear lateral expansion, as shown in Figure 36 (a), and expressed as

$$k_a = \frac{F}{\Delta l} \quad (\text{Eqn. 26})$$

Where F is the force acted on the nanosheet to expand it while Δl is the linear extension. To calculate out the area expansion modulus, the force-extension data has been traced during the biaxial stretching process. The fitted data shows k_a of the nanosheet is $3.44 \times 10^2 \mu N / m$.

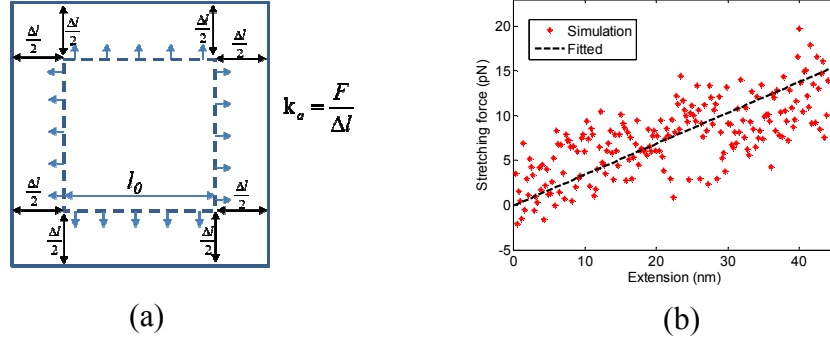


Figure 36. (a) Definition of area expansion modulus. (b) Force-strain curve of the nanosheet during area expansion

Shear modulus (η) of the nanosheet is defined as the ratio of shear stress (τ_{xy}) to shear strain (γ_{xy}):

$$\eta = \frac{\tau_{xy}}{\gamma_{xy}} = \frac{F / A}{\tan(\Delta\theta)} \quad (\text{Eqn. 27})$$

where shear stress (τ_{xy}) is the ratio of force (F_s) and A is the area on which the force acts, $\Delta\theta$ is the shear degree, whose definition has been depicted in Figure 37 (a); shear strain equals $\tan(\Delta\theta)$. To obtain the shear modulus, the shear force-shear strain relationship has been traced during the shearing process of the first nanosheet, as shown in Figure 37 (b). The shear modulus turns out to be $6.07 \times 10^4 Pa$, detailed calculation can be found in the Supporting Information.

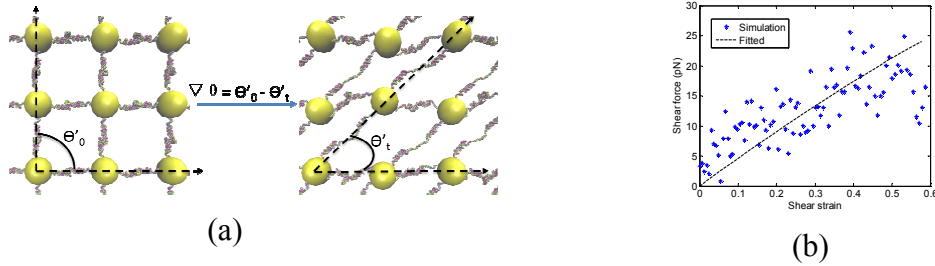


Figure 37. (a) Definition of shear degree. (b) Shear force-shear degree curve of the nanosheet

It should be noted that the both area expansion modulus and shear modulus of the nanosheet are determined by its structural parameters such as sequences, number of bases in hairpin loop and bar sections and number of connections between each NP. They are also weakly dependent on the temperature and salt concentration. The relationship between these parameters and k_a as well as η is similar to that between these parameters with F_{un} and F_{ru} , detailed discussion can be found in the Supporting Information.

4.4. Conclusions

A CGMD model for a 2D nanosheet which is assembled by DNA-gold nanoparticle conjugates have been established to test mechanical properties of the nanosheet and its feasibility of serving as nano strain sensor. Compared to other strain sensors, this nanosheet distinguishes itself by the fact that it can be utilized on flexible surface of a freely moving arbitrary shaped structure under complex environments. The model has been validated by the good agreement between the indentation response of nanosheet and stretching properties of hairpin structure obtained from our model with those reported by literature.

The feasibility of applying nanosheet as strain sensor has been tested by biaxial stretching and shearing tests. It is found that the force needed to rupture the structure is 4 times larger than that to elastically deform it. Thus, a safe force range ensured the potential of operating nanosheet to deform elastically without rupturing it. Numerical models are also established for calculating safe operating force range and are verified by simulations. Effects of physical conditions such as the temperature and salt concentration on mechanical properties of the 2D lattice have been included in the numerical model. In summary, the

feasibility, reproducibility and reliability of this 2D lattice to serve as a strain sensor have been proved.

Mechanical properties of nanosheet, such as area expansion modulus and shear modulus, have been obtained from the model. The area expansion modulus of the nanosheet is approximately $3.44 \times 10^2 \mu N/m$ while the shear modulus is $6.07 \times 10^4 Pa$. Future work includes the experimental validation of mechanical properties of nanosheet and its application to quantify strains of cells under different loading conditions.

4.5. Acknowledgements

The authors acknowledge the supports for this work from National Science Foundation Grant Nos. CBET-1067502 and CBET-1113040 for Y.L..

REFERENCES

1. Rackus, D.G., et al., *A digital microfluidic device with integrated nanostructured microelectrodes for electrochemical immunoassays*. Lab on a Chip, 2015.
2. Cheng, Y., et al., *Design of biocompatible dendrimers for cancer diagnosis and therapy: current status and future perspectives*. Chemical Society Reviews, 2011. **40**(5): p. 2673-2703.
3. Zhou, Y., et al., *Biomarker Binding on an Antibody-Functionalized Biosensor Surface: The Influence of Surface Properties, Electric Field, and Coating Density*. The Journal of Physical Chemistry C, 2014. **118**(26): p. 14586-14594.
4. Peng, B., et al., *Modeling Nanoparticle Targeting to a Vascular Surface in Shear Flow Through Diffusive Particle Dynamics*. Nanoscale Research Letters, 2015. **10**(1): p. 1-9.
5. Wang, S., et al., *Computational modeling of magnetic nanoparticle targeting to stent surface under high gradient field*. Computational Mechanics, 2014. **53**(3): p. 403-412.
6. Liu, Y., et al., *Structure Design of Vascular Stents*, in *Multiscale Simulations and Mechanics of Biological Materials*. 2013, John Wiley & Sons Ltd. p. 301-317.
7. Ercolessi, F., *A molecular dynamics primer*. Springer College in Computational Physics, 1997.
8. Levitt, M., *Computer simulation of protein folding*. Abstracts of Papers of the American Chemical Society, 1998. **216**: p. U636-U636.
9. Kamerlin, S.C.L., et al., *Coarse-Grained (Multiscale) Simulations in Studies of Biophysical and Chemical Systems*. Annual Review of Physical Chemistry, Vol 62, 2011. **62**: p. 41-64.
10. Johnston, K. and V. Harmandaris, *Hierarchical Multiscale Modeling of Polymer–Solid Interfaces: Atomistic to Coarse-Grained Description and Structural and Conformational Properties of Polystyrene–Gold Systems*. Macromolecules, 2013. **46**(14): p. 5741-5750.
11. Steve, C. and J.B. Markus, *Coarse-Graining Parameterization and Multiscale Simulation of Hierarchical Systems. Part I*, in *Multiscale Modeling*, 2010, CRC Press. p. 13-34.
12. Marrink, S.J., et al., *The MARTINI Force Field: Coarse Grained Model for Biomolecular Simulations*. The Journal of Physical Chemistry B, 2007. **111**(27): p. 7812-7824.
13. Shih, A.Y., et al., *Coarse grained protein-lipid model with application to lipoprotein particles*. Journal of Physical Chemistry B, 2006. **110**(8): p. 3674-3684.
14. Payne, M.C., et al., *Iterative minimization techniques for ab initio total-energy calculations: molecular dynamics and conjugate gradients*. Reviews of Modern Physics, 1992. **64**(4): p. 1045-1097.
15. Park, J.-K., R. Jernigan, and Z. Wu, *Coarse Grained Normal Mode Analysis vs. Refined Gaussian Network Model for Protein Residue-Level Structural Fluctuations*. Bulletin of Mathematical Biology, 2013. **75**(1): p. 124-160.
16. Gruhl, F., B. Rapp, and K. Länge, *Biosensors for Diagnostic Applications*, in *Molecular Diagnostics*, H. Seitz and S. Schumacher, Editors. 2013, Springer Berlin Heidelberg. p. 115-148.
17. Malhotra, B.D. and A. Chaubey, *Biosensors for clinical diagnostics industry*. Sensors and Actuators B: Chemical, 2003. **91**(1–3): p. 117-127.
18. Mascini, M. and S. Tombelli, *Biosensors for biomarkers in medical diagnostics*. Biomarkers, 2008. **13**(7-8): p. 637-657.

19. Liu, Y., et al., *Biospecies Capture and Detection at Low Concentration*. Micro and Nanosystems, 2012. **4**(4): p. 254-272.
20. Liu, Y.L., et al., *Electrokinetic effects on detection time of nanowire biosensor*. Applied Physics Letters, 2012. **100**(15).
21. Tian, R., et al., *Ultrasensitive protein detection using lithographically defined Si multi-nanowire field effect transistors*. Lab on a Chip, 2011. **11**(11): p. 1952-1961.
22. Kozack, R.E., M.J. d'Mello, and S. Subramaniam, *Computer modeling of electrostatic steering and orientational effects in antibody-antigen association*. Biophysical Journal, 1995. **68**(3): p. 807-814.
23. Vashist, S.K., et al., *Effect of antibody immobilization strategies on the analytical performance of a surface plasmon resonance-based immunoassay*. Analyst, 2011. **136**(21): p. 4431-4436.
24. Squires, T.M., R.J. Messinger, and S.R. Manalis, *Making it stick: convection, reaction and diffusion in surface-based biosensors*. Nature Biotechnology, 2008. **26**(4): p. 417-426.
25. Chen, S.F., et al., *Controlling antibody orientation on charged self-assembled monolayers*. Langmuir, 2003. **19**(7): p. 2859-2864.
26. Zhou, J., et al., *Monte Carlo simulations of antibody adsorption and orientation on charged surfaces*. Journal of Chemical Physics, 2004. **121**(2): p. 1050-1057.
27. Kim, Y.-P., et al., *Electrochemical glucose biosensor by electrostatic binding of PQQ-glucose dehydrogenase onto self-assembled monolayers on gold*. Journal of Applied Electrochemistry, 2012. **42**(6): p. 383-390.
28. Josephs, E.A. and T. Ye, *Electric-Field Dependent Conformations of Single DNA Molecules on a Model Biosensor Surface*. Nano Letters, 2012. **12**(10): p. 5255-5261.
29. Bergström, G. and C.-F. Mandenius, *Orientation and capturing of antibody affinity ligands: Applications to surface plasmon resonance biochips*. Sensors and Actuators B: Chemical, 2011. **158**(1): p. 265-270.
30. Schramm, W., S.-H. Paek, and G. Voss, *Strategies for the Immobilization of Antibodies*. ImmunoMethods, 1993. **3**(2): p. 93-103.
31. Lu, B., M.R. Smyth, and R. O'Kennedy, *Tutorial review. Oriented immobilization of antibodies and its applications in immunoassays and immunosensors*. Analyst, 1996. **121**(3): p. 29R-32R.
32. Qian, W.P., et al., *Immobilization of antibodies on ultraflat polystyrene surfaces*. Clinical Chemistry, 2000. **46**(9): p. 1456-1463.
33. Sorci, M., et al., *Oriented Covalent Immobilization of Antibodies for Measurement of Intermolecular Binding Forces between Zipper-Like Contact Surfaces of Split Inteins*. Analytical Chemistry, 2013. **85**(12): p. 6080-6088.
34. Chaudhri, A., et al., *Coarse-Grained Modeling of the Self-Association of Therapeutic Monoclonal Antibodies*. Journal of Physical Chemistry B, 2012. **116**(28): p. 8045-8057.
35. Chaudhri, A., et al., *The Role of Amino Acid Sequence in the Self-Association of Therapeutic Monoclonal Antibodies: Insights from Coarse-Grained Modeling*. Journal of Physical Chemistry B, 2013. **117**(5): p. 1269-1279.
36. Gunnar Bergstrom, C.-F.M., *orientation and capturing of antibody affinity ligands: applications to surface plasmon resonance biochips*. Sensors and Actuators B: Chemical, 2011. **158**(1): p. 265-270.

37. Orgovan, N., et al., *Dependence of cancer cell adhesion kinetics on integrin ligand surface density measured by a high-throughput label-free resonant waveguide grating biosensor*. Scientific Reports, 2014. **4**.
38. Nordenfelt, P., et al., *Antibody orientation at bacterial surfaces is related to invasive infection*. Journal of Experimental Medicine, 2012. **209**(13): p. 2367-2381.
39. Dhanekar, S. and S. Jain, *Porous silicon biosensor: Current status*. Biosensors and Bioelectronics, 2013. **41**(0): p. 54-64.
40. Schlichtiger, A., et al., *Covalent attachment of functionalized cardiolipin on a biosensor gold surface allows repetitive measurements of anticardiolipin antibodies in serum*. Analytical and Bioanalytical Chemistry, 2013. **405**(1): p. 275-285.
41. Mroczkowski, S.J., *CONTRIBUTION OF SURFACE PROPERTIES TO ANTIBODY IMMOBILIZATION*. Department of Health and Human Services, 1987.
42. Peluso, P., et al., *Optimizing antibody immobilization strategies for the construction of protein microarrays*. Analytical Biochemistry, 2003. **312**(2): p. 113-124.
43. Trilling, A.K., J. Beekwilder, and H. Zuilhof, *Antibody orientation on biosensor surfaces: a minireview*. Analyst, 2013. **138**(6): p. 1619-1627.
44. Tian, R.H., et al., *Ultrasensitive protein detection using lithographically defined Si multi-nanowire field effect transistors*. Lab on a Chip, 2011. **11**(11): p. 1952-1961.
45. Aswal, D.K., et al., *Self assembled monolayers on silicon for molecular electronics*. Analytica Chimica Acta, 2006. **568**(1-2): p. 84-108.
46. Love, J.C., et al., *Self-assembled monolayers of thiolates on metals as a form of nanotechnology*. Chemical Reviews, 2005. **105**(4): p. 1103-1169.
47. Tajima, N., M. Takai, and K. Ishihara, *Significance of Antibody Orientation Unraveled: Well-Oriented Antibodies Recorded High Binding Affinity*. Analytical Chemistry, 2011. **83**(6): p. 1969-1976.
48. Conroy, P.J., et al., *Antibody production, design and use for biosensor-based applications*. Seminars In Cell & Developmental Biology, 2009. **20**(1): p. 10-26.
49. Zeng, X.Q., Z.H. Shen, and R. Mernaugh, *Recombinant antibodies and their use in biosensors*. Analytical And Bioanalytical Chemistry, 2012. **402**(10): p. 3027-3038.
50. Deasy, B., et al., *Development Of an Antibody-Based Biosensor for Determination Of 7-Hydroxycoumarin (Umbelliferone) Using Horseradish-Peroxidase Labeled Anti-7-Hydroxycoumarin Antibody*. Analytica Chimica Acta, 1994. **294**(3): p. 291-297.
51. Deasy, B., et al., *Development of an antibody-based biosensor for determination of 7-hydroxycoumarin (umbelliferone) using horseradish peroxidase labelled anti-7-hydroxycoumarin antibody*. Analytica Chimica Acta, 1994. **294**(3): p. 291-297.
52. Hall, W.P., S.N. Ngatia, and R.P. Van Duyne, *LSPR Biosensor Signal Enhancement Using Nanoparticle–Antibody Conjugates*. The Journal of Physical Chemistry C, 2011. **115**(5): p. 1410-1414.
53. Lilyestrom, W., et al., *Crystal structure of SV40 large T-antigen bound to p53: interplay between a viral oncoprotein and a cellular tumor suppressor*. Genes & Development, 2006. **20**(17): p. 2373-2382.
54. Matthew, J.B., *Electrostatic Effects In Proteins*. Annual Review Of Biophysics And Biophysical Chemistry, 1985. **14**: p. 387-417.

55. Mehler, E.L. and T. Solmajer, *Electrostatic effects in proteins: comparison of dielectric and charge models*. Protein Engineering, 1991. **4**(8): p. 903-910.
56. Jiang, N. and J. Ma, *Multi-layer coarse-graining polarization model for treating electrostatic interactions of solvated alpha-conotoxin peptides*. Journal Of Chemical Physics, 2012. **136**(13).
57. Sharp, K.A. and B. Honig, *Electrostatic Interactions In Macromolecules - Theory And Applications*. Annual Review Of Biophysics And Biophysical Chemistry, 1990. **19**: p. 301-332.
58. Schutz, C.N. and A. Warshel, *What are the dielectric "constants" of proteins and how to validate electrostatic models?* Proteins-Structure Function And Genetics, 2001. **44**(4): p. 400-417.
59. Kriel, L.A., *Development of Antibodies Specific for Binding New Biomarkers of Exposure to Cholinesterase Inhibitors*. Department of Health and Human Services, 2013.
60. Einstein, A., *Investigations on the Theory of Brownian Movement* Dover, 1956.
61. Saltzman, W.M., et al., *Antibody Diffusion in Human Cervical-Mucus*. Biophysical Journal, 1994. **66**(2): p. 508-515.
62. Iima, M., et al., *Apparent Diffusion Coefficient as an MR Imaging Biomarker of Low-Risk Ductal Carcinoma in Situ: A Pilot Study*. Radiology, 2011. **260**(2): p. 364-372.
63. Novotny, J., R.E. Bruccoleri, and F.A. Saul, *On the Attribution Of Binding-Energy In Antigen-Antibody Complexes Mcpc-603, D1.3, And Hybel-5*. Biochemistry, 1989. **28**(11): p. 4735-4749.
64. Standard, J.M., *Energy Minimization Method*. Chemistry, 2013. **380**(37).
65. Brandt, J.P., T.W. Patapoff, and S.R. Aragon, *Construction, MD Simulation, and Hydrodynamic Validation of an All-Atom Model of a Monoclonal IgG Antibody*. Biophysical Journal, 2010. **99**(3): p. 905-913.
66. Ken Takahashi, T.O., Keiji Naruse *Coarse-grained molecular dynamics simulations of biomolecules*. AIMS Biophysics, 2014. **1**(1): p. 1-15.
67. Chi, Q., et al., *Ordered Assembly and Controlled Electron Transfer of the Blue Copper Protein Azurin at Gold (111) Single-Crystal Substrates*. The Journal of Physical Chemistry B, 2001. **105**(20): p. 4669-4679.
68. Plimpton, S., *Fast Parallel Algorithms for Short-Range Molecular Dynamics*. Journal of Computational Physics, 1995. **117**(1): p. 1-19.
69. Wiseman, M.E. and C.W. Frank, *Antibody adsorption and orientation on hydrophobic surfaces*. Langmuir, 2012. **28**(3): p. 1765-74.
70. Zaremba, L.A., *Guidance for Industry and FDA Staff: Criteria for Significant Risk Investigations of Magnetic Resonance Diagnostic Devices*. Center for Devices and Radiological Health, 2003.
71. Liu, W., et al., *Crystalline Two-Dimensional DNA-Origami Arrays*. Angewandte Chemie, 2011. **123**(1): p. 278-281.
72. Liu, Y., et al., *Thermodynamic Analysis of Nylon Nucleic Acids*. ChemBioChem, 2008. **9**(10): p. 1641-1648.
73. Wang, R., C. Nuckolls, and S.J. Wind, *Assembly of Heterogeneous Functional Nanomaterials on DNA Origami Scaffolds*. Angewandte Chemie International Edition, 2012. **51**(45): p. 11325-11327.

74. Cutler, J.I., E. Auyeung, and C.A. Mirkin, *Spherical Nucleic Acids*. Journal Of the American Chemical Society, 2012. **134**(3): p. 1376-1391.
75. Delong, R.K., et al., *Functionalized gold nanoparticles for the binding, stabilization, and delivery of therapeutic DNA, RNA, and other biological macromolecules*. Nanotechnol Sci Appl, 2010. **3**: p. 53-63.
76. Li, Z., et al., *Multiple thiol-anchor capped DNA-gold nanoparticle conjugates*. Nucleic Acids Res, 2002. **30**(7): p. 1558-62.
77. Niemeyer, C.M., et al., *Bifunctional DNA-gold nanoparticle conjugates as building blocks for the self-assembly of cross-linked particle layers*. Biochemical and Biophysical Research Communications, 2003. **311**(4): p. 995-999.
78. Young, K.L., et al., *Hollow Spherical Nucleic Acids for Intracellular Gene Regulation Based upon Biocompatible Silica Shells*. Nano Letters, 2012. **12**(7): p. 3867-3871.
79. Auyeung, E., et al., *DNA-mediated nanoparticle crystallization into Wulff polyhedra*. Nature, 2014. **505**(7481): p. 73-77.
80. Tan, S.J., et al., *Crystallization of DNA-Capped Gold Nanoparticles in High-Concentration, Divalent Salt Environments*. Angewandte Chemie International Edition, 2014. **53**(5): p. 1316-1319.
81. Doyen, M., K. Bartik, and G. Bruylants, *DNA-Promoted Auto-Assembly of Gold Nanoparticles: Effect of the DNA Sequence on the Stability of the Assemblies*. Polymers, 2013. **5**(3): p. 1041-1055.
82. Park, S.Y., et al., *DNA-programmable nanoparticle crystallization*. Nature, 2008. **451**(7178): p. 553-556.
83. Nykypanchuk, D., et al., *DNA-guided crystallization of colloidal nanoparticles*. Nature, 2008. **451**(7178): p. 549-552.
84. Mirkin, C.A., et al., *A DNA-based method for rationally assembling nanoparticles into macroscopic materials*. Nature, 1996. **382**(6592): p. 607-609.
85. Jones, M.R., et al., *DNA-nanoparticle superlattices formed from anisotropic building blocks*. Nat Mater, 2010. **9**(11): p. 913-917.
86. Daniel, M.C. and D. Astruc, *Gold nanoparticles: Assembly, supramolecular chemistry, quantum-size-related properties, and applications toward biology, catalysis, and nanotechnology*. Chemical Reviews, 2004. **104**(1): p. 293-346.
87. Sonnichsen, C., et al., *A molecular ruler based on plasmon coupling of single gold and silver nanoparticles*. Nat Biotech, 2005. **23**(6): p. 741-745.
88. Sato, K., K. Hosokawa, and M. Maeda, *Rapid Aggregation of Gold Nanoparticles Induced by Non-Cross-Linking DNA Hybridization*. Journal of the American Chemical Society, 2003. **125**(27): p. 8102-8103.
89. Stoeva, S.I., et al., *Three-Layer Composite Magnetic Nanoparticle Probes for DNA*. Journal of the American Chemical Society, 2005. **127**(44): p. 15362-15363.
90. Kouassi, G.K. and J. Irudayaraj, *Magnetic and Gold-Coated Magnetic Nanoparticles as a DNA Sensor*. Analytical Chemistry, 2006. **78**(10): p. 3234-3241.
91. Sharma, J., et al., *Control of Self-Assembly of DNA Tubules Through Integration of Gold Nanoparticles*. Science, 2009. **323**(5910): p. 112-116.
92. Li, H. and L.J. Rothberg, *DNA Sequence Detection Using Selective Fluorescence Quenching of Tagged Oligonucleotide Probes by Gold Nanoparticles*. Analytical Chemistry, 2004. **76**(18): p. 5414-5417.

93. Taton, T.A., C.A. Mirkin, and R.L. Letsinger, *Scanometric DNA Array Detection with Nanoparticle Probes*. *Science*, 2000. **289**(5485): p. 1757-1760.
94. Rosi, N.L., et al., *Oligonucleotide-Modified Gold Nanoparticles for Intracellular Gene Regulation*. *Science*, 2006. **312**(5776): p. 1027-1030.
95. Dulkeith, E., et al., *Gold Nanoparticles Quench Fluorescence by Phase Induced Radiative Rate Suppression*. *Nano Letters*, 2005. **5**(4): p. 585-589.
96. Kundu, S. and M. Jayachandran, *The self-assembling of DNA-templated Au nanoparticles into nanowires and their enhanced SERS and catalytic applications*. *RSC Advances*, 2013. **3**(37): p. 16486-16498.
97. Cao, Y.C., R. Jin, and C.A. Mirkin, *Nanoparticles with Raman Spectroscopic Fingerprints for DNA and RNA Detection*. *Science*, 2002. **297**(5586): p. 1536-1540.
98. Liu, J. and Y. Lu, *A Colorimetric Lead Biosensor Using DNAzyme-Directed Assembly of Gold Nanoparticles*. *Journal of the American Chemical Society*, 2003. **125**(22): p. 6642-6643.
99. Zheng, X., et al., *Catalytic Gold Nanoparticles for Nanoplasmonic Detection of DNA Hybridization*. *Angewandte Chemie*, 2011. **123**(50): p. 12200-12204.
100. Elghanian, R., et al., *Selective Colorimetric Detection of Polynucleotides Based on the Distance-Dependent Optical Properties of Gold Nanoparticles*. *Science*, 1997. **277**(5329): p. 1078-1081.
101. Storhoff, J.J., et al., *What Controls the Optical Properties of DNA-Linked Gold Nanoparticle Assemblies?* *Journal of the American Chemical Society*, 2000. **122**(19): p. 4640-4650.
102. Cutler, J.I., et al., *Polyvalent Nucleic Acid Nanostructures*. *Journal Of the American Chemical Society*, 2011. **133**(24): p. 9254-9257.
103. Srivastava, S., et al., *Two-Dimensional DNA-Programmable Assembly of Nanoparticles at Liquid Interfaces*. *Journal of the American Chemical Society*, 2014. **136**(23): p. 8323-8332.
104. Srinivasan, B., et al., *Designing DNA-grafted particles that self-assemble into desired crystalline structures using the genetic algorithm*. *Proceedings of the National Academy of Sciences*, 2013. **110**(46): p. 18431-18435.
105. Chi, C., et al., *Internal Structure of Nanoparticle Dimers Linked by DNA*. *Acs Nano*, 2012. **6**(8): p. 6793-6802.
106. Zhang, Y., et al., *A general strategy for the DNA-mediated self-assembly of functional nanoparticles into heterogeneous systems*. *Nat Nano*, 2013. **8**(11): p. 865-872.
107. Li, D., J. Rogers, and S.L. Biswal, *Probing the Stability of Magnetically Assembled DNA-Linked Colloidal Chains*. *Langmuir*, 2009. **25**(16): p. 8944-8950.
108. Byrom, J., et al., *Directing Assembly of DNA-Coated Colloids with Magnetic Fields To Generate Rigid, Semiflexible, and Flexible Chains*. *Langmuir*, 2014. **30**(30): p. 9045-9052.
109. Prigodich, A.E., et al., *Tailoring DNA Structure To Increase Target Hybridization Kinetics on Surfaces*. *Journal Of the American Chemical Society*, 2010. **132**(31): p. 10638-10641.
110. Hurst, S.J., H.D. Hill, and C.A. Mirkin, *"Three-Dimensional Hybridization" with polyvalent DNA-gold nanoparticle conjugates*. *Journal Of the American Chemical Society*, 2008. **130**(36): p. 12192-12200.
111. Giljohann, D.A., et al., *Gene Regulation with Polyvalent siRNA-Nanoparticle Conjugates*. *Journal Of the American Chemical Society*, 2009. **131**(6): p. 2072-+.
112. Jensen, S.A., et al., *Spherical Nucleic Acid Nanoparticle Conjugates as an RNAi-Based Therapy for Glioblastoma*. *Science Translational Medicine*, 2013. **5**(209): p. 209ra152.

113. Georganopoulou, D.G., et al., *Nanoparticle-based detection in cerebral spinal fluid of a soluble pathogenic biomarker for Alzheimer's disease*. Proceedings Of the National Academy Of Sciences Of the United States Of America, 2005. **102**(7): p. 2273-2276.
114. Kim, E.Y., et al., *Detection of HIV-1 p24 Gag in plasma by a nanoparticle-based bio-barcode-amplification method*. Nanomedicine, 2008. **3**(3): p. 293-303.
115. Tang, S.X., et al., *Nanoparticle-based biobarcode amplification assay (BCA) for sensitive and early detection of human immunodeficiency type 1 capsid (p24) antigen*. Jaids-Journal Of Acquired Immune Deficiency Syndromes, 2007. **46**(2): p. 231-237.
116. Lefferts, J.A., P. Jannetto, and G.J. Tsongalis, *Evaluation of the Nanosphere Verigene (R) System and the Verigene (R) F5/F2/MTHFR Nucleic Acid Tests*. Experimental And Molecular Pathology, 2009. **87**(2): p. 105-108.
117. Storhoff, J., et al., *Detection of prostate cancer recurrence using an ultrasensitive nanoparticle-based PSA assay*. Journal Of Clinical Oncology, 2009. **27**(15).
118. Seferos, D.S., et al., *Nano-flares: Probes for transfection and mRNA detection in living cells*. Journal Of the American Chemical Society, 2007. **129**(50): p. 15477-+.
119. Lytton-Jean, A.K.R. and C.A. Mirkin, *A thermodynamic investigation into the binding properties of DNA functionalized gold nanoparticle probes and molecular fluorophore probes*. Journal Of the American Chemical Society, 2005. **127**(37): p. 12754-12755.
120. Ding, Y.J. and J. Mittal, *Insights into DNA-mediated interparticle interactions from a coarse-grained model*. Journal Of Chemical Physics, 2014. **141**(18).
121. Chou, L.Y.T., K. Zagorovsky, and W.C.W. Chan, *DNA assembly of nanoparticle superstructures for controlled biological delivery and elimination*. Nat Nano, 2014. **9**(2): p. 148-155.
122. Zhao, P., et al., *Molecular Nanoworm with PCL Core and PEO Shell as a Non-spherical Carrier for Drug Delivery*. Macromolecular Rapid Communications, 2012. **33**(16): p. 1351-1355.
123. Park, J.H., et al., *Magnetic iron oxide nanoworms for tumor targeting and imaging*. Advanced Materials, 2008. **20**(9): p. 1630-+.
124. Aluri, S.R., et al., *A Hybrid Protein-Polymer Nanoworm Potentiates Apoptosis Better than a Monoclonal Antibody*. ACS Nano, 2014. **8**(3): p. 2064-2076.
125. Park, J.H., et al., *Cooperative nanomaterial system to sensitize, target, and treat tumors*. Proceedings Of the National Academy Of Sciences Of the United States Of America, 2010. **107**(3): p. 981-986.
126. Mandal, S., et al., *Therapeutic nanoworms: towards novel synthetic dendritic cells for immunotherapy*. Chemical Science, 2013. **4**(11): p. 4168-4174.
127. Auyeung, E., et al., *Synthetically programmable nanoparticle superlattices using a hollow three-dimensional spacer approach*. Nature Nanotechnology, 2012. **7**(1): p. 24-28.
128. Byrom, J., et al., *Directing Assembly of DNA-Coated Colloids with Magnetic Fields To Generate Rigid, Semiflexible, and Flexible Chains*. Langmuir, 2014. **30**(30): p. 9045-52.
129. Moghimi, S.M., A.C. Hunter, and J.C. Murray, *Long-circulating and target-specific nanoparticles: Theory to practice*. Pharmacological Reviews, 2001. **53**(2): p. 283-318.
130. Knotts, T.A., et al., *A coarse grain model for DNA*. Journal Of Chemical Physics, 2007. **126**(8).

131. Padovan-Merhar, O., F.V. Lara, and F.W. Starr, *Stability of DNA-linked nanoparticle crystals: Effect of number of strands, core size, and rigidity of strand attachment*. Journal Of Chemical Physics, 2011. **134**(24).
132. Vargas Lara, F. and F.W. Starr, *Stability of DNA-linked nanoparticle crystals I: Effect of linker sequence and length*. Soft Matter, 2011. **7**(5): p. 2085-2093.
133. Zwanikken, J.W., et al., *Local Ionic Environment around Polyvalent Nucleic Acid-Functionalized Nanoparticles*. The Journal of Physical Chemistry C, 2011. **115**(33): p. 16368-16373.
134. Harnau, L., R.G. Winkler, and P. Reineker, *Dynamic Properties Of Molecular Chains with Variable Stiffness*. Journal Of Chemical Physics, 1995. **102**(19): p. 7750-7757.
135. Dhakal, S., et al., *Growth Dynamics for DNA-Guided Nanoparticle Crystallization*. ACS Nano, 2013. **7**(12): p. 10948-10959.
136. Lee, O.S., T.R. Prytkova, and G.C. Schatz, *Using DNA to Link Gold Nanoparticles, Polymers, and Molecules: A Theoretical Perspective*. Journal Of Physical Chemistry Letters, 2010. **1**(12): p. 1781-1788.
137. Macfarlane, R.J., et al., *Nanoparticle Superlattice Engineering with DNA*. Science, 2011. **334**(6053): p. 204-208.
138. Lee, O.-S. and G. Schatz, *Computational Simulations of the Interaction of Lipid Membranes with DNA-Functionalized Gold Nanoparticles*, in *Biomedical Nanotechnology*, S.J. Hurst, Editor. 2011, Humana Press. p. 283-296.
139. Lee, O.S., V.Y. Cho, and G.C. Schatz, *A- to B-Form Transition in DNA Between Gold Surfaces*. Journal Of Physical Chemistry B, 2012. **116**(23): p. 7000-7005.
140. Lee, O.S. and G.C. Schatz, *Computational Studies Of the Properties Of DNA-Linked Nanomaterials*. Advances In Chemical Physics, Vol 149, 2012. **149**: p. 197-249.
141. Liu, W.K., et al., *An introduction to computational nanomechanics and materials*. Computer Methods in Applied Mechanics and Engineering, 2004. **193**(17–20): p. 1529-1578.
142. Leventis, N., et al., *Polymer nanoencapsulated mesoporous vanadia with unusual ductility at cryogenic temperatures*. Journal Of Materials Chemistry, 2008. **18**(21): p. 2475-2482.
143. Hinckley, D.M., et al., *An experimentally-informed coarse-grained 3-site-per-nucleotide model of DNA: Structure, thermodynamics, and dynamics of hybridization*. Journal Of Chemical Physics, 2013. **139**(14).
144. Plimpton, S., *Fast Parallel Algorithms for Short-Range Molecular-Dynamics*. Journal Of Computational Physics, 1995. **117**(1): p. 1-19.
145. Sambriski, E.J., D.C. Schwartz, and J.J. de Pablo, *A Mesoscale Model of DNA and Its Renaturation*. Biophysical Journal, 2009. **96**(5): p. 1675-1690.
146. Pu, Q., et al., *Molecular dynamics simulations of stretched gold nanowires: The relative utility of different semiempirical potentials*. The Journal of Chemical Physics, 2007. **126**(14): p. 144707.
147. Cossaro, A., et al., *X-ray diffraction and computation yield the structure of alkanethiols on gold(111)*. Science, 2008. **321**(5891): p. 943-946.
148. Ramachandran, A., et al., *Coarse-grained molecular dynamics simulation of DNA translocation in chemically modified nanopores*. J Phys Chem B, 2011. **115**(19): p. 6138-48.
149. Ohno, S., *Intrinsic Evolution Of Proteins - the Role Of Peptidic Palindromes*. Rivista Di Biologia-Biology Forum, 1990. **83**(2-3): p. 405-410.

150. Piana, S., *Structure and energy of a DNA dodecamer under tensile load*. Nucleic Acids Research, 2005. **33**(22): p. 7029-7038.
151. Hückel, P.D.a.E., *The theory of electrolytes. I. Lowering of freezing point and related phenomena*. Physikalische Zeitschrift, 1923. **24**: p. 185-206.
152. Stoller, P., V. Jacobsen, and V. Sandoghdar, *Measurement of the complex dielectric constant of a single gold nanoparticle*. Optics Letters, 2006. **31**(16): p. 2474-2476.
153. Heeder, N., et al., *Electrical Behavior of Carbon Nanotube Reinforced Epoxy under Compression*, in *Dynamic Behavior of Materials, Volume 1*, T. Proulx, Editor. 2011, Springer New York. p. 361-368.
154. Cheng, W., et al., *Free-standing nanoparticle superlattice sheets controlled by DNA*. Nat Mater, 2009. **8**(6): p. 519-525.
155. Mueggenburg, K.E., et al., *Elastic membranes of close-packed nanoparticle arrays*. Nat Mater, 2007. **6**(9): p. 656-660.
156. Montrichok, A., G. Gruner, and G. Zocchi, *Trapping intermediates in the melting transition of DNA oligomers*. Europhysics Letters, 2003. **62**(3): p. 452-458.
157. Hill, H.D., et al., *The Role Radius of Curvature Plays in Thiolated Oligonucleotide Loading on Gold Nanoparticles*. ACS Nano, 2009. **3**(2): p. 418-424.
158. Barrow, S.J., et al., *Surface Plasmon Resonances in Strongly Coupled Gold Nanosphere Chains from Monomer to Hexamer*. Nano Letters, 2011. **11**(10): p. 4180-4187.
159. Lo, J.H., et al., *Nanoparticle amplification via photothermal unveiling of cryptic collagen binding sites*. Journal of Materials Chemistry B, 2013. **1**(39): p. 5235-5240.
160. Zhou, J., et al., *Nanoparticle-Based Delivery of RNAi Therapeutics: Progress and Challenges*. Pharmaceuticals (Basel), 2013. **6**(1): p. 85-107.
161. Li, D., S. Banon, and S.L. Biswal, *Bending dynamics of DNA-linked colloidal particle chains*. Soft Matter, 2010. **6**(17): p. 4197-4204.
162. Klinkova, A., et al., *Structural and Optical Properties of Self-Assembled Chains of Plasmonic Nanocubes*. Nano Letters, 2014. **14**(11): p. 6314-6321.
163. Loweth, C.J., et al., *DNA-based assembly of gold nanocrystals*. Angewandte Chemie-International Edition, 1999. **38**(12): p. 1808-1812.
164. Lalander, C.H., et al., *DNA-Directed Self-Assembly of Gold Nanoparticles onto Nanopatterned Surfaces: Controlled Placement of Individual Nanoparticles into Regular Arrays*. ACS Nano, 2010. **4**(10): p. 6153-6161.
165. Roberts, N.A., et al., *Directed Assembly of One- and Two-Dimensional Nanoparticle Arrays from Pulsed Laser Induced Dewetting of Square Waveforms*. ACS Applied Materials & Interfaces, 2013. **5**(10): p. 4450-4456.
166. Zheng, J., et al., *Two-Dimensional Nanoparticle Arrays Show the Organizational Power of Robust DNA Motifs*. Nano Letters, 2006. **6**(7): p. 1502-1504.
167. Xiao, S., et al., *Selfassembly of Metallic Nanoparticle Arrays by DNA Scaffolding*. Journal of Nanoparticle Research, 2002. **4**(4): p. 313-317.
168. Hill, H.D., et al., *Controlling the Lattice Parameters of Gold Nanoparticle FCC Crystals with Duplex DNA Linkers*. Nano Letters, 2008. **8**(8): p. 2341-2344.
169. Kim, J.-Y. and J.-S. Lee, *Synthesis and Thermally Reversible Assembly of DNA-Gold Nanoparticle Cluster Conjugates*. Nano Letters, 2009. **9**(12): p. 4564-4569.
170. Zanchet, D., et al., *Electrophoretic Isolation of Discrete Au Nanocrystal/DNA Conjugates*. Nano Letters, 2000. **1**(1): p. 32-35.

171. Maye, M.M., et al., *Switching binary states of nanoparticle superlattices and dimer clusters by DNA strands*. Nat Nano, 2010. **5**(2): p. 116-120.
172. Shemer, G., et al., *Chirality of Silver Nanoparticles Synthesized on DNA*. Journal of the American Chemical Society, 2006. **128**(34): p. 11006-11007.
173. Tan, S.J., et al., *Building plasmonic nanostructures with DNA*. Nat Nano, 2011. **6**(5): p. 268-276.
174. Santhanam, V., et al., *Self-Assembly of Uniform Monolayer Arrays of Nanoparticles*. Langmuir, 2003. **19**(19): p. 7881-7887.
175. Murray, C.B., D.J. Norris, and M.G. Bawendi, *Synthesis and characterization of nearly monodisperse CdE (E = sulfur, selenium, tellurium) semiconductor nanocrystallites*. Journal of the American Chemical Society, 1993. **115**(19): p. 8706-8715.
176. Murray, C.B., et al., *Colloidal synthesis of nanocrystals and nanocrystal superlattices*. IBM J. Res. Dev., 2001. **45**(1): p. 47-56.
177. Andres, R.P., et al., *Self-assembly of a two-dimensional superlattice of molecularly linked metal clusters*. Science, 1996. **273**(5282): p. 1690-1693.
178. Giersig, M. and P. Mulvaney, *Formation of ordered two-dimensional gold colloid lattices by electrophoretic deposition*. The Journal of Physical Chemistry, 1993. **97**(24): p. 6334-6336.
179. Trau, M., D.A. Saville, and I.A. Aksay, *Field-Induced Layering of Colloidal Crystals*. Science, 1996. **272**(5262): p. 706-709.
180. Grabar, K.C., et al., *Two-Dimensional Arrays of Colloidal Gold Particles: A Flexible Approach to Macroscopic Metal Surfaces*. Langmuir, 1996. **12**(10): p. 2353-2361.
181. Rubin, S., et al., *Novel approach for the preparation of metal colloid monolayers on modified surfaces*. Journal of Vacuum Science & Technology A: Vacuum, Surfaces, and Films, 1996. **14**(3): p. 1870-1877.
182. Sato, T., D.G. Hasko, and H. Ahmed, *Nanoscale colloidal particles: Monolayer organization and patterning*. Journal of Vacuum Science & Technology B: Microelectronics and Nanometer Structures, 1997. **15**(1): p. 45-48.
183. Sato David Brown, T. and B. F. G. Johnson, *Nucleation and growth of nano-gold colloidal lattices*. Chemical Communications, 1997(11): p. 1007-1008.
184. Bolat, G., et al., *Fabrication of a Polyaniline Ultramicroelectrode via a Self Assembled Monolayer Modified Gold Electrode*. Sensors, 2013. **13**(7): p. 8079-8094.
185. Lee, W.-Y., et al., *Electron Hopping and Electronic Conductivity in Monolayers of Alkanethiol-Stabilized Gold Nano-Clusters at the Air/Water Interface*. Israel Journal of Chemistry, 1997. **37**(2-3): p. 213-223.
186. Schmid, G. and N. Beyer, *A New Approach to Well-Ordered Quantum Dots*. European Journal of Inorganic Chemistry, 2000. **2000**(5): p. 835-837.
187. Jahn, S., N. Geerts, and E. Eiser, *DNA-Mediated Two-Dimensional Colloidal Crystallization above Different Attractive Surfaces*. Langmuir, 2010. **26**(22): p. 16921-16927.
188. Guedon, C.M., et al., *Controlling the interparticle distance in a 2D molecule-nanoparticle network*. Nanotechnology, 2011. **22**(12): p. 125205.
189. Zou, B., et al., *Self-assembly of crosslinked DNA-gold nanoparticle layers visualized by in-situ scanning force microscopy*. Advanced Materials, 2005. **17**(13): p. 1643-+.
190. Srivastava, S., et al., *Tunable Nanoparticle Arrays at Charged Interfaces*. Acs Nano, 2014. **8**(10): p. 9857-9866.

191. Liao, J., et al., *Reversible formation of molecular junctions in 2D nanoparticle arrays*. *Advanced Materials*, 2006. **18**(18): p. 2444-+.
192. Chee, M., et al., *Accessing genetic information with high-density DNA arrays*. *Science*, 1996. **274**(5287): p. 610-614.
193. Reichert, J., et al., *Chip-based optical detection of DNA hybridization by means of nanobead labeling*. *Analytical Chemistry*, 2000. **72**(24): p. 6025-6029.
194. Chuntanov, L. and G. Haran, *Optical activity in single-molecule surface-enhanced Raman scattering: Role of symmetry*. *MRS Bulletin*, 2013. **38**(08): p. 642-647.
195. Brandl, D.W., N.A. Mirin, and P. Nordlander, *Plasmon Modes of Nanosphere Trimers and Quadrumers*. *The Journal of Physical Chemistry B*, 2006. **110**(25): p. 12302-12310.
196. Hong, Y. and B.M. Reinhard, *Collective photonic-plasmonic resonances in noble metal - dielectric nanoparticle hybrid arrays*. *Optical Materials Express*, 2014. **4**(11): p. 2409-2422.
197. Geerts, N. and E. Eiser, *DNA-functionalized colloids: Physical properties and applications*. *Soft Matter*, 2010. **6**(19): p. 4647-4660.
198. Lobkovsky, A., et al., *Scaling Properties Of Stretching Ridges In a Crumpled Elastic Sheet*. *Science*, 1995. **270**(5241): p. 1482-1485.
199. Gupta, A.N., et al., *Experimental validation of free-energy-landscape reconstruction from non-equilibrium single-molecule force spectroscopy measurements*. *Nature Physics*, 2011. **7**(8): p. 631-634.
200. Naserian-Nik, A.M., M. Tahani, and M. Karttunen, *Molecular dynamics study of DNA oligomers under angled pulling*. *Rsc Advances*, 2014. **4**(21): p. 10751-10760.
201. Lenormand, G., et al., *Direct Measurement of the Area Expansion and Shear Moduli of the Human Red Blood Cell Membrane Skeleton*. *Biophysical Journal*. **81**(1): p. 43-56.

Vita

Personal Information

Name Yihua Zhou
Place of Birth Chongqing, China
Date of Birth March 25, 1990
Father Zhiqing Zhou *Mother* Kaiyu Hu

Educations

Lehigh university 08/2015
Ph.D. in Mechanical Engineering
Harbin Institute of Technology 07/2011
B.Eng. in Material Science and Technology

Publications

- (1) Zhou, Y.; Sohrabi, S.; Tan, J.; Liu, Y., Mechanical properties of nanoworm assembled by DNA and nanoparticle conjugates. *Journal of Nanoscience and Nanotechnology* 2015, 15, 6617-6620.
- (2) Peng, B.; Liu, Y.; Zhou, Y.; Yang, L.; Zhang, G.; Liu, Y., Modeling Nanoparticle Targeting to a Vascular Surface in Shear Flow through Diffusive Particle Dynamics. *Nanoscale Research Letters* 2015, 10, 235.
- (3) Zhou, Y.; Hu, W.; Peng, B.; Liu, Y., Biomarker Binding on an Antibody-Functionalized Biosensor Surface: The Influence of Surface Properties, Electric Field, and Coating Density. *The Journal of Physical Chemistry C* 2014, 118 (26), 14586-14594.
- (4) Wang, S.; Zhou, Y.; Tan, J.; Xu, J.; Yang, J.; Liu, Y., Computational modeling of magnetic nanoparticle targeting to stent surface under high gradient field. *Computational mechanics* 2014, 53 (3), 403-412.
- (5) Zhou, Y.; Liu, Y.; Mechanical properties and applications of nanostructures by DNA-AuNP conjugates. *The 7th World Congress of Biomechanics* 2014.
- (6) Liu, Y.; Yang, J.; Zhou, Y.; Hu, J., Structure Design of Vascular Stents. In *Multiscale Simulations and Mechanics of Biological Materials*, John Wiley & Sons Ltd: 2013; pp 301-317.

Professional Experience

- (1) Worked as Student Engineer in *Enterprise System Center* during 09/11~12/11
- (2) Interned as Manufacturing Operator in *First Automobile Workshop* during 09/10~10/10
- (3) Interned as Mechanical Designer in *Chang'an Automobile* during 09/10~10/10
- (4) Certified in Six Sigma and Engineer-In-Training